Clays and Clay Minerals, Vol. 68, No. 4:394–412, 2020

THE EFFECT OF THE STARTING MINERALOGICAL MIXTURE ON THE NATURE OF Fe-SERPENTINES OBTAINED DURING HYDROTHERMAL SYNTHESIS AT 90°C

Isabella Pignatelli[1]*, Régine Mosser-Ruck[1], Enrico Mugnaioli[2], Jérôme Sterpenich[1], and Mauro Gemmi[2]

[1]Georessources UMR 7359 CNRS-UL, Université de Lorraine, BP 70239, 54506 Vandœuvre-lès-Nancy, Cedex, France
[2]Center for Nanotechnology Innovation@NEST, Istituto Italiano di Tecnologia, Piazza San Silvestro 12, 56127 Pisa, Italy

Abstract—The formation conditions and stability fields of Fe-serpentines are still poorly understood in both terrestrial (natural or anthropic) and extraterrestrial environments. Knowledge of the effects of physical-chemical parameters on compositional and structural features of Fe-serpentines is lacking, and only a few thermodynamic parameters of these minerals are available in the literature. To fill these gaps, the synthesis of these minerals, while controlling all the physicochemical experimental parameters, was undertaken. Two hydrothermal syntheses were carried out at 90°C to investigate the effect of two different starting mineralogical mixtures on the nature of Fe-serpentines. The run products were identified by several analytical techniques (powder X-ray diffraction, transmission, and scanning electron microscopy). Berthierine crystals were synthesized from a starting mixture of kaolinite and metal iron. The berthierines synthesized show different morphologies and iron contents (~3–38 at.%). From a starting mineralogical mixture composed of quartz and metal iron, cronstedtite crystallizes. Most of the crystals are 1*M* polytypes. Magnetite is always associated with both berthierine and cronstedtite. Lepidocrocite was observed only in the experiment with kaolinite. These experimental results demonstrated that Fe enrichment in serpentines depends on the silicate precursor (kaolinite or quartz) of the starting mixture. The results are also in agreement with the geochemical equilibrium predicted by thermodynamic modeling, i.e. the formation of berthierine and cronstedtite in association with magnetite at the expense of metal iron and silicates.

Keywords—Berthierine · Cronstedtite · Fe-serpentines · Hydrothermal synthesis

INTRODUCTION

Berthierine, cronstedtite, greenalite, and odinite are Fe-bearing serpentines, phyllosilicate minerals which consist of a tetrahedral and an octahedral sheet (T–O or 1:1 layer). Their general formula is $M_3T_2O_5(OH)_4$, where T are the tetrahedral sites generally occupied by Si^{4+} and Al^{3+} and *M* are divalent or trivalent cations in octahedral coordination, such as Fe^{3+}, Fe^{2+}, Al^{3+}, Mg^{2+}. The octahedral sheet contains three *M* sites but the presence of cations with different oxidation states or valences implies an intermediate occupancy between di- and trioctahedral for most of them.

Cronstedtite $(Fe^{2+}_{3-x}\ Fe^{3+}_{x})(Si_{2-x}\ Fe^{3+}_{x})O_5(OH)_4$ is an exception because: (1) there are no vacant sites in the octahedral sheet; and (2) it contains tetrahedrally coordinated Fe^{3+} (Bailey 1969; Geiger et al. 1983; Smrčok et al. 1994; Hybler et al. 2000, 2002; Kogure et al. 2002). The same features are shown by a rare Fe-bearing serpentine, guidottiite, the Mn-analogue of cronstedtite with the formula $(Mn_{1.86}Fe^{3+}_{0.61}Mg_{0.54})(Si_{1.36}Fe^{3+}_{0.64})O_5(OH)_4$ (Wahle et al. 2010).

Fe-serpentines form during fluid–rock interactions in both extraterrestrial and terrestrial environments. In the terrestrial one, these minerals can be formed in natural and anthropic contexts. On Earth, greenalite $(Fe^{2+}_{a}Fe^{3+}_{b}Mg_{c}\square_{d})_{\Sigma=3}Si_2O_5(OH)_4$ ($a > b$ and $(a + b) > (c + d)$; Guggenheim et al. 1982) occurs in metamorphosed Archean banded-iron formations at $T < 450$°C (Gole 1980a, 1980b), where it may have precipitated under anoxic, ferruginous, marine conditions (Tosca et al. 2016). Odinite $(R^{3+}_{a}R^{2+}_{b}\square_{c})_{\Sigma=3}(Si_{2-x}\ Al_x)O_5(OH)_4$ (with $a > b$, R^{3+} and R^{2+} dominantly Fe and Mg, respectively) is believed to form at 25°C in marine waters at the sediment–water interface (Bailey 1988). It occurs in shallow marine shelfs and reef lagoonal areas in tropical latitudes where it is associated with biogenic carbonate and fluviatile systems. This mineral is not found in sediments older than Recent due to its alterability to chlorite (Bailey 1988). Berthierine $(R^{2+}_{a}R^{3+}_{b}\square_{c})_{\Sigma=3}(Si_{2-x}\ Al_x)O_5(OH)_4$ (Brindley 1982) is found in marine and brackish oolitic ironstone formations (Hornibrook and Longstaffe 1996). It can form by the diagenetic transformation of kaolinite under slightly alkaline conditions at $T < 160$°C (Iijima and Matsumoto 1982; Bhattacharyya 1983). Berthierine can also form by hydrothermal and diagenetic processes in a marine sedimentary exhalative environment where it is associated with siderite, organic matter, and magnetite (Rivas-Sanchez et al. 2006). Cronstedtite is observed in low-*T* hydrothermal veins associated with pyrite, quartz, carbonates (siderite, calcite), and sphalerite (Frondel 1962; López-García et al. 1992; Hybler et al. 2016, 2017).

Fe-serpentines are found also on other bodies of the Solar System. Berthierine crystals have been found in the Nakhla Martian meteorite as an alteration product of melt inclusion glasses within olivine phenocrysts (Lee and Chatzitheodoris 2016). These crystals are Al depleted and Fe enriched in comparison to terrestrial berthierine due to an interstratification with another Fe-serpentine, likely greenalite. A serpentine containing only ferric iron and with composition similar to that

* E-mail address of corresponding author: isabella.pignatelli@univ-lorraine.fr
DOI: 10.1007/s42860-020-00080-y

of odinite occurred in the mesostasis fractures of Martian meteorite, Lafayette (Hicks et al. 2014). A complex mixture of Fe-phyllosilicates is also found within veins and mesostasis of this Martian meteorite, and TEM data are consistent with a mixture of a Fe-smectite with Fe-serpentines having a berthierine-type composition (Changela and Bridges 2011). Visible and near-infrared spectroscopic data suggested the occurrence of: (1) cronstedtite and greenalite in some dark regions of Mars (Calvin 1998); (2) cronstedtite on the dwarf planet Ceres (Zolotov 2014); and (3) berthierine in CI and CM meteorites such as Orgueil, Murchison, and Murray (Calvin and King 1997). Other analytical techniques (electron probe microanalysis - EPMA, scanning and transmission electron microscopy – SEM/TEM) confirmed the presence of Fe-serpentine, in particular cronstedtite and greenalite, in both the fine-rims and the matrices of CM meteorites where they are mixed with Mg-serpentines (Barber 1981; Browning et al. 1996; Lauretta et al. 2000; Elmaleh et al. 2012, 2015). Cronstedtite crystals also occur in pseudomorphs after olivine and pyroxene of a CM meteorite known as Paris (Pignatelli et al. 2016, 2017, 2018).

In the anthropic context, thermodynamic modeling and experimental data predicted the formation of Fe-serpentines during iron–clay interactions simulating the conditions of radioactive-waste disposal facilities in multi-barrier systems (e.g. Wilson et al. 2006; Mosser-Ruck et al. 2010; de Combarieu et al. 2011; Pignatelli et al. 2014, etc.). Although many studies have been carried out during the last 20 years, the formation of Fe-serpentines is still under investigation because it could modify the chemical, physical, and mechanical properties of clay barriers with time (Bildstein et al. 2006).

Whatever the environment, the formation conditions and the stability fields of Fe-serpentines are poorly understood, although it is important that they be reconstructed so that the fluid–rock interactions and the chemical environments during the evolution of Earth and other bodies of the Solar System are better understood better (Zolensky and Keller 1999). In particular, there is a lack of knowledge about the effects of physical-chemical parameters (temperature, fluid composition, water/solid ratio, etc.) on compositional and structural features of Fe-serpentines, above all on cation substitutions. This knowledge is fundamental for comparing terrestrial and extraterrestrial Fe-serpentines in order to check if their similarities are simply fortuitous, or, on the contrary, they can give important information about analogous processes in both environments (Zolensky 1984).

The main objectives of this study were (1) to synthesize Fe-serpentines using a new procedure (two different silicate precursors, rather than gels, in a chloride solution at 90°C); (2) to investigate the effect of the two different starting mineralogical mixtures on the nature of Fe-serpentines; and (3) to compare the experimental run products with geochemical equilibria calculated by thermodynamic modeling.

MATERIALS AND METHODS

Batch experiments were carried out using Parr® non/stirred pressure vessels (Parr Instrument Company, Moline, Illinois, USA) made of Teflon® (capacity of 23 mL) at a temperature of 90°C. The samples were labeled K90 and Q90 because the starting mineralogical mixtures were made, respectively, of kaolinite (1 g) or Fontainebleau sandstone (1 g), each mixed with 500 mg of metal iron powder to give a mass ratio of 0.5. A commercial kaolinite supplied by Sigma-Aldrich Co. (Darmstadt, Germany; Catalog #K7375; Ø 0.1–0.4 μm) and Fontainebleau sandstone were used. Minerals rather than gels were used as starting materials to better simulate the fluid–rock interactions occurring in natural and anthropic environments, as well as to favor the formation of well crystalline serpentines. The Fontainebleau sandstone was chosen because it is composed almost entirely of quartz, with traces of clay minerals (kaolinite, illite, smectite), feldspars, calcite, siderite, and chalcedony (SiO_2 = 99.5% – Kreutzer et al. 2017; Saadi et al. 2017). Powdered metal iron with a purity of 99.9% and mean grain size of 40 μm was provided by Sigma Aldrich. The starting mixtures were prepared in a glove box under inert argon atmosphere and added to a chlorine solution with $pH_{25°C}$ = 6.4 (NaCl 22 mmol L^{-1} + $CaCl_2$ 2.9 mmol L^{-1}) in agreement with previous studies on Fe-serpentine formation (Guillaume et al. 2003; Mosser-Ruck et al. 2010; Pignatelli et al. 2013; Rivard et al. 2013a; Bourdelle et al. 2014, 2017). A solution having the same composition was used because the dissolution of silicates is enhanced by the presence of alkaline or alkaline earth cations (e.g. Dove and Crerar 1990; Dove and Elston 1992; Dove et al. 2005). Silicate dissolution releases Si in solution, thus favoring the formation of Fe-serpentines. Both solution/kaolinite and solution/sandstone ratios were fixed at 10.

After 75 days, the vessels were opened in a glove box and prepared for analysis. The pH of the run solutions was measured, after cooling at room temperature, using a combination of a silver/sulfide electrode and 0.025 μm filtration. The accuracy of the pH measurement is 0.1. The electrode was calibrated using reference buffer solutions with pH 4, 7, and 10 certified by the Physikalisch-Technische Bundesanstalt (PTB, Germany) and the National Institute of Standards and Technology (NIST, USA). The run solutions were diluted ten times in 2 vol.% HNO_3 and analyzed at SARM laboratory (Université de Lorraine, France) by inductively coupled plasma optical emission spectroscopy (ICP-OES) with a Thermo Scientific iCAP 6500 spectrometer (Thermo Scientific, Waltham, Massachusetts, USA) to determine the concentrations of Si, Fe, and Al.

Powder X-ray diffraction (PXRD) was used to analyze the bulk run products (dried under an argon flux in the glove box) in order to identify the newly formed minerals. X-ray patterns were collected at LIEC laboratory (Université de Lorraine, France) at room temperature with a D8 Bruker diffractometer (Bruker, Billerica, Massachusetts, USA) using CoKα radiation (λ = 1.7902 Å), 35 kV accelerating voltage and 45 mA beam current. The analytical conditions of data collection were: scan step of 0.035°2θ, exposure time of 3 s, $2\theta_{min}$ = 3° to $2\theta_{max}$ = 74°. Scanning electron microscopy was used to obtain secondary electron (SE) and backscattered electron (BSE) images of run products, as well as energy dispersive X-ray (EDX) spectra. Both images and spectra were recorded at SCMEM laboratory

https://doi.org/10.1007/s42860-020-00080-y Published online by Cambridge University Press

(Université de Lorraine, France) using a Hitachi S-4800 (Hitachi, Tokyo, Japan) cold field emission gun with an accelerating voltage of 15 kV and a beam current of 10 nA.

Transmission electron microscopy (TEM) was used to analyze the <2 μm fraction of run products. A drop of this fraction was dispersed in ethanol under ultrasonication (Fisherbrand™ S-Series Ultrasonic Cleaner, Thermo Fisher Scientific, Waltham, Massachusetts, USA) for a period of 3 min and then evaporated on a carbon film of a 200 mesh copper grid. The EDX spectra and three-dimensional electron diffraction (3D ED; Kolb et al. 2011; Mugnaioli and Gemmi 2018; Gemmi et al. 2019) were performed at the Center for Nanotechnology Innovation@NEST (Pisa, Italy) using a Zeiss Libra TEM (Zeiss, Jena, Germany) operating at 120 kV and equipped with a LaB_6 source and a Bruker EDS detector XFlash6T-60. The EDX data were collected using a probe diameter of ~100 nm and a counting time of 60–120 s. K_{AB} factors were determined without standards using the thin-specimen approximation of Cliff and Lorimer (1975).

3D ED acquisitions were done in STEM mode after defocusing the beam in order to have pseudo-parallel illumination of the sample. A beam diameter of ~150 nm was obtained by inserting a 5 μm C2 condenser aperture. An extremely mild illumination was adopted in order to avoid any alteration or amorphization of the sample during the 3D ED experiments. 3D ED was performed with a processing beam obtained by a Nanomegas Digistar P1000 device (Nanomegas, Brussels, Belgium). The precession semi-angle was kept at 1°. Independent data sets were recorded for each phase, with acquisition tilt ranges of ±40° and tilt step of 1°. Camera length was kept at 180 mm, with an actual resolution in reciprocal space of 0.75 Å. Conventional ED and 3D ED data were recorded using an ASI Timepix detector (Amsterdam Scientific Instruments, Amsterdam, The Netherlands), which was able to record the arrival of single electrons and deliver a pattern that is virtually background-free. These data were analyzed using *ADT3D* (Kolb et al. 2011) and in-house developed *MATLAB* routines.

Thermodynamic modeling was carried out using *PHREEQC* code (Parkhurst and Appelo 1999) in conjunction with the Thermoddem database of the BRGM institute (*Thermoddem V1.10* Code version 1.07_2.06, 2014). In that database, the cronstedtite formula is $Fe^{2+}{}_3(SiAl)O_5(OH)_4$, however, and it does not correspond to the correct one $(Fe^{2+}{}_{3-x}Fe^{3+}{}_x)(Si_{2-x}Fe^{3+}{}_x)O_5(OH)_4$ with $0 < x < 0.8$ (Geiger et al. 1983; Smrčok et al. 1994; Hybler et al. 2000, 2002; Kogure et al. 2002). Because of its Al content and the absence of iron in the tetrahedral sites, as well as the presence of only Fe^{2+}, the composition and thermodynamic data of cronstedtite reported by Wolery and Jove-Colon (2004) was used as previously by Zolotov (2014).

RESULTS

Kaolinite + Fe^0 Experiment (K90)

After heating at 90°C, the PXRD pattern underlined the slight decrease in reflection intensities for both kaolinite and metal iron in comparison to the starting sample (Fig. 1a), as well as the appearance of new reflections, corresponding to magnetite (35.1, 41.3, and 67.3°2θ, i.e. d_{hkl} 2.97, 2.53, and 1.62 Å) and lepidocrocite (16.4 and 31.5°2θ, i.e. d_{hkl} 6.28 and 3.30 Å). A more detailed analysis of the run product PXRD pattern showed other changes for the main kaolinite reflections: the reflection at 14.2°2θ (7.25 Å) shifted slightly toward higher angles and became broader, whereas that at 28.7°2θ (3.61 Å) showed a shoulder at 29.1°2θ (3.56 Å). These changes can be attributed to a loss of crystallinity, a partial dissolution of kaolinite, and the presence of new T–O phyllosilicates.

This was confirmed by the appearance of a small reflection at 38.3°2θ (2.72 Å) and by the decompositions of two regions on PXRD patterns performed using *DECOMPXR* software (Lanson 1997). This software allows for the subtraction of background and the decomposition of superimposed reflections into elementary ones with Gaussian and Lorentzian shapes (Lanson and Besson 1992; Lanson 1997). In the 13–15°2θ region of the PXRD pattern of the starting sample, the decomposition did not need more than one reflection at 14.2°2θ (7.25 Å), i.e. that of kaolinite, to obtain the best fit. At 90°C, the decomposition underlined the presence of two reflections: that of kaolinite at 14.2°2θ (7.25 Å) and a weaker one at 14.3°2θ (7.19 Å) corresponding to newly formed T–O phyllosilicates (Fig. 2).

Observations by SEM and semi-quantitative SEM-EDX analysis showed that T–O phyllosilicates were characterized by several morphologies and they differed from kaolinite in the presence of both Al and Fe (Fig. 3). Fe, Al, and Si contents were measured by TEM-EDX and plotted in a ternary diagram (Fig. 4). Newly formed T–O particles showed various Fe contents varying from ~3 to 38 atomic %. Particles enriched in Fe (~60–80 at. %) were also observed. The distribution field of all analyzed particles fell between the poles of kaolinite and berthierine, although the most Fe-enriched particles were closer to the cronstedtite pole. The linear trend representing the particles' composition was very close to the ideal one corresponding to the evolution of kaolinite toward cronstedtite, i.e. the most Fe-rich T–O phyllosilicate (Fig. 4).

Fontainebleau Sandstone + Fe^0 Experiment (Q90)

The PXRD pattern of run products showed the formation of Fe-bearing minerals, i.e. magnetite and T–O phyllosilicates (reflections at 14.5 and 29.1°2θ, i.e. d_{hkl} 7.13 and 3.55 Å – Fig. 1b). The crystals of newly formed T–O phyllosilicates were characterized by a pyramidal morphology with triangular or pseudo-hexagonal cross-sections. The latter were bigger and less abundant on SEM images (Fig. 5a,b). Few conical crystals were observed (Fig. 5d). These crystals contain only Si, Fe, and O (Fig. 5c). Their morphology is similar to that of natural terrestrial and extraterrestrial cronstedtite crystals (Hybler et al. 2000; Kogure et al. 2002; Pignatelli et al. 2018), and those synthetised by Pignatelli et al. (2013, 2014) from an experiment simulating the interaction of a claystone with iron between 90°C and 40°C.

The TEM-EDX data plotted in Fig. 6 were used to calculate the structural formula of cronstedtite pyramidal crystals, on the basis of 5 cations and adjusting the Fe^{3+}/Fe^{2+} ratio to obtain electroneutrality. The average formula is:

https://doi.org/10.1007/s42860-020-00080-y Published online by Cambridge University Press

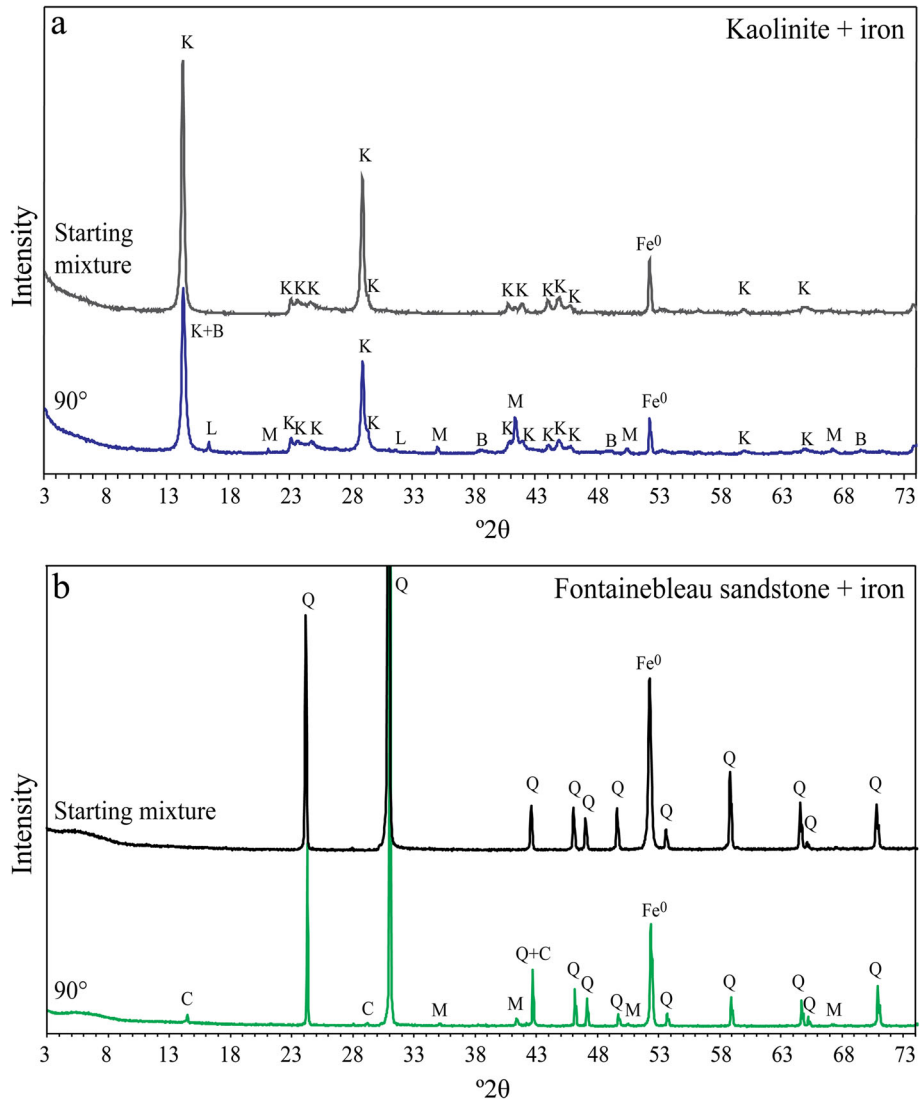

Fig. 1. a PXRD patterns of kaolin-iron starting mixture with a mass ratio kaolinite/iron of 0.5 (gray line) and run product at 90°C (blue line). **b** PXRD patterns of Fontainebleau sandstone-iron starting mixture with a mass ratio sandstone/iron of 0.5 (black line) and run product at 90°C (green line). K = kaolinite, M = magnetite, L = lepidocrocite, B = berthierine, Q = quartz, C = cronstedtite, Fe^0 = metal iron

$$\left(Fe^{2+}{}_{2.3}Fe^{3+}{}_{0.7}\right)\left(Si_{1.3}Fe^{3+}{}_{0.7}\right)O_5(OH)_4$$

The SAED patterns of cronstedtite crystals showed that some of them were characterized by streaking along the c^* axis typical of the stacking disorder in the polytypical sequence (Fig. 7d). Among the most ordered ones, 3D ED measurements enabled the identification of a 1*M* polytype by comparing 2D sections of the reconstructed 3D reciprocal space (Fig. 7) with the identification diagram for cronstedtite polytypes available in the literature (Smrčok and Weiss 1993; Ďurovič 1997; Hybler et al. 2008, 2018). In fact, the spot distribution along the [11*l*]* row on the $(hhl_{hex})^*$ plane suggested that the polytype belongs to Bailey's group A (Bailey 1969), whereas the spot distribution on the $(h0l_{hex})^*$ and $(h0l_{hex})^*$ planes corresponded to those of group I and II on the identification diagram. Moreover, 3D ED data indicated that the polytype is monoclinic with a *C*-centered cell and parameters $a = 5.4(1)$ Å, and $b = 9.3(2)$ Å, $c = 7.4(1)$ Å, and $\beta = 104.9(5)°$, in agreement with the space group *Cm* of 1*M* polytype (Steadman and Nuttall 1964; Hybler 2014).

The SEM and TEM images also showed the presence of foil-like particles (Figs 8 and 9). These particles were nanocrystalline or amorphous as revealed by the presence of diffuse rings with few sharp diffraction spots in the SAED

https://doi.org/10.1007/s42860-020-00080-y Published online by Cambridge University Press

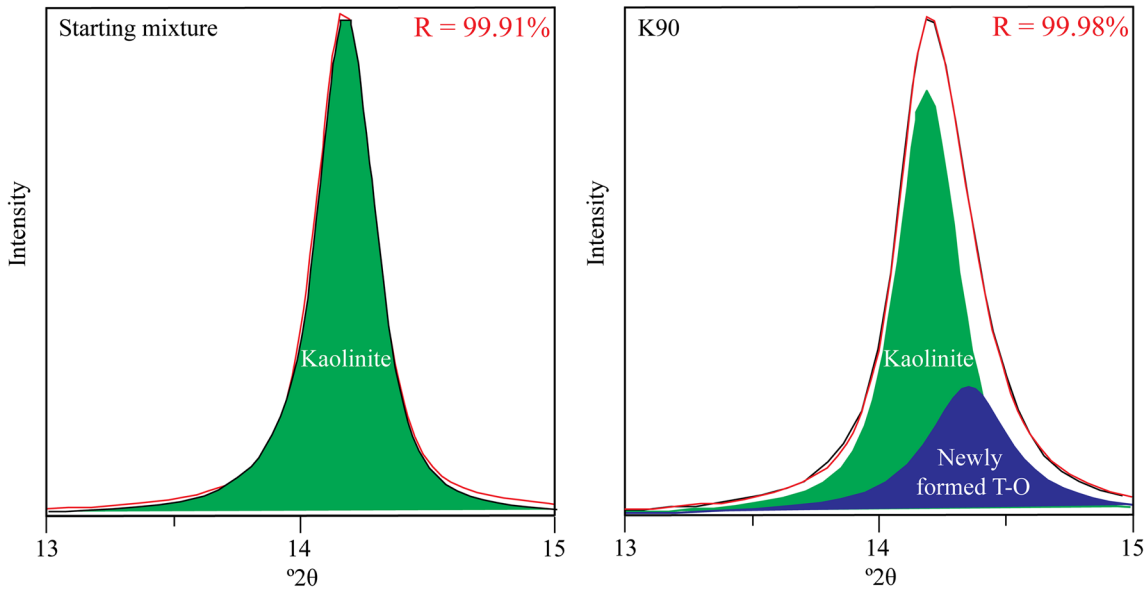

Fig. 2. Decomposition of PXRD patterns in the range 13–15°2θ for the starting mixture and run product of K90 experiment. Black line = experimental pattern, red line = fitting

patterns. Their indexation gave d_{hkl} values of ~4.8–4.5, 2.7, 2.5, and 1.5 Å and an angle of ~60° between the directions [100]* and [010]* (Fig. 9c, d, and e). These data are compatible with those of T–O phyllosilicates.

The compositions of foil-like particles were characterized by greater Si contents than those of cronstedtite crystals, which varied from ~34 to 38 at.% (Fig. 8). Their compositions were intermediate between those of cronstedtite and greenalite (Fig. 6). The average structural formula of these particles can be written as:

$$\left(Fe^{2+}{}_{2.8}Fe^{3+}{}_{0.2}\right)\left(Si_{1.8}Fe^{3+}{}_{0.2}\right)O_5(OH)_4$$

From the compositional point of view, these particles can be considered as being cronstedtite because they do not contain enough Si to fill the tetrahedral sites and consequently a small amount of Fe^{3+} is hypothesized to be present.

Run Solution Analysis

Very small amounts of Fe, Al, and Si were measured in the run solutions (<2 mg/L for K90 and <9 ml/L for Q90 – Table 1) and this suggests that almost all were incorporated into the structures of newly formed Fe serpentines (berthierine and cronstedtite) and also in iron (oxyhydr)oxides.

The presence of Al in the solution of experiment Q90 is likely due to the dissolution of trace minerals present in the Fontainebleau sandstone, such as clay minerals and feldspars (Kreutzer et al. 2017; Saadi et al. 2017).

Both the K90 and Q90 run solutions were supersaturated with respect to iron (oxyhydr)oxides other than magnetite and lepidocrocite (such as ferrihydrite, goethite, green rusts), but they were not detected analytically. However, the nucleation of metastable, poorly crystalline nanometric phases, for example ferrihydrite, during the experiment and/or the autoclave cooling cannot be excluded. According to the literature, when iron oxidizes in the presence of water, ferrihydrite is formed at first and it can transform to more thermodynamically stable hematite or goethite (Cudennec and Lecerf 2006; Liu et al. 2007). Although the run solutions were filtered before analysis, nanoparticles of ferrihydrite could pass through the filter and be present in the solutions, explaining why such amounts of iron were detected.

Thermodynamic Simulations

Thermodynamic tests were performed using *PHREEQC* software to simulate the following experimental observations: (1) kaolinite transformation into berthierine and more Fe-rich serpentines, such as greenalite or cronstedtite, associated with magnetite and lepidocrocite in experiment K90; (2) cronstedtite and magnetite formation in experiment Q90. The composition of the initial solution was simulated by adding Ca, Na, and Cl in the amounts described in the section "Materials and Methods", pH and pe were free to evolve, whereas the gas volume was fixed at 13 mL (taking into account the volume occupied by the solids and the solution in the autoclave).

A first simulation test at 90°C for both K90 and Q90 experiments consisted of reacting minerals with the aqueous solution to determine T–O phyllosilicates and iron (oxyhydr)oxides for which the solution presents a positive saturation index and are thus able to precipitate under the experimental conditions.

For experiment K90, they are greenalite, Fe^{2+}-berthierine, Fe^{3+}-berthierine, cronstedtite, magnetite, and lepidocrocite. The

https://doi.org/10.1007/s42860-020-00080-y Published online by Cambridge University Press

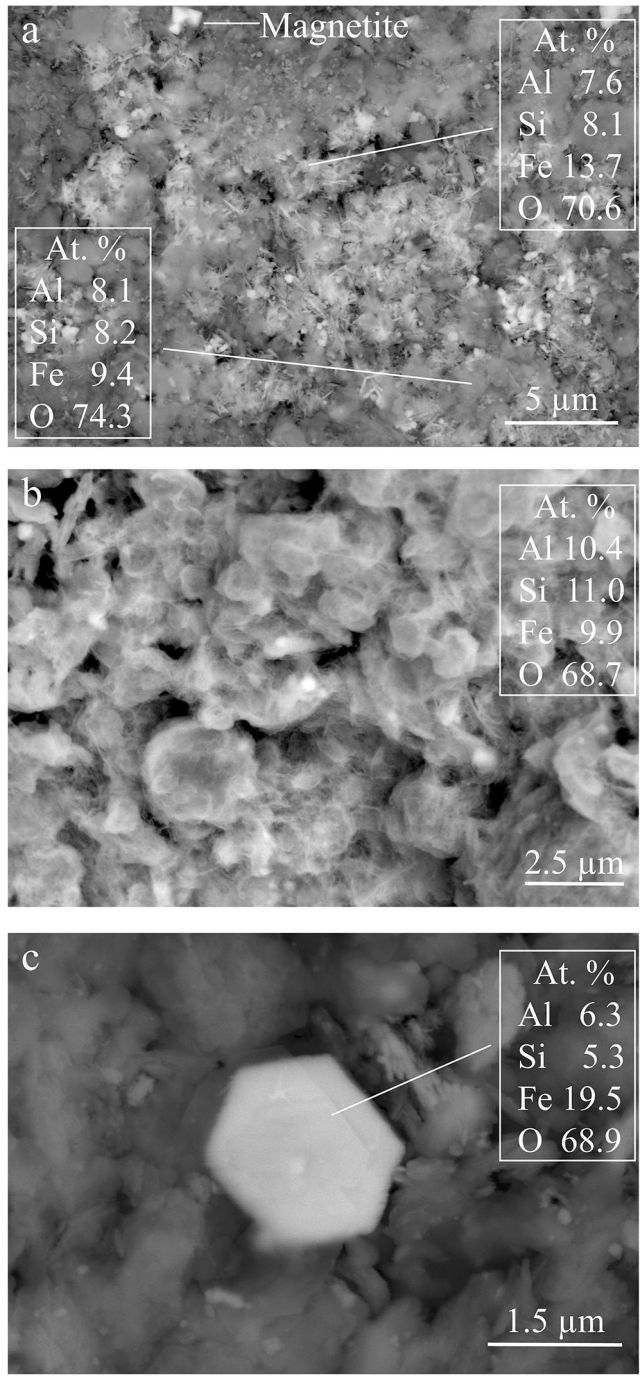

Fig. 3. BSE-SEM images and EDX data of run products in experiment K90. **a** Magnetite crystals mixed with newly formed T–O phyllosilicates. Other morphologies of T–O phyllosilicates characterized by **b** small and **c** large iron contents, respectively

solution is also over-saturated with respect to hematite and ferrihydrite, but they were not observed in the run products and thus were ignored in the first modeling. In the second simulation test, these minerals were able to precipitate. The results showed that kaolinite is partially dissolved (0.0024 moles), in agreement with the experimental results (Fig. 1a), and the final $pH_{90°C}$ was 7.02. Magnetite and lepidocrocite did not crystallize, nor did Fe^{3+}-berthierine. Although equilibrium is achieved in the model when all iron has been consumed, iron was still present in the run product at the end of the experiment (Fig. 1a). The modeling allowed for Fe^{2+}-berthierine and greenalite precipitation rather than cronstedtite. The most Fe-rich T–O phyllosilicates analyzed

https://doi.org/10.1007/s42860-020-00080-y Published online by Cambridge University Press

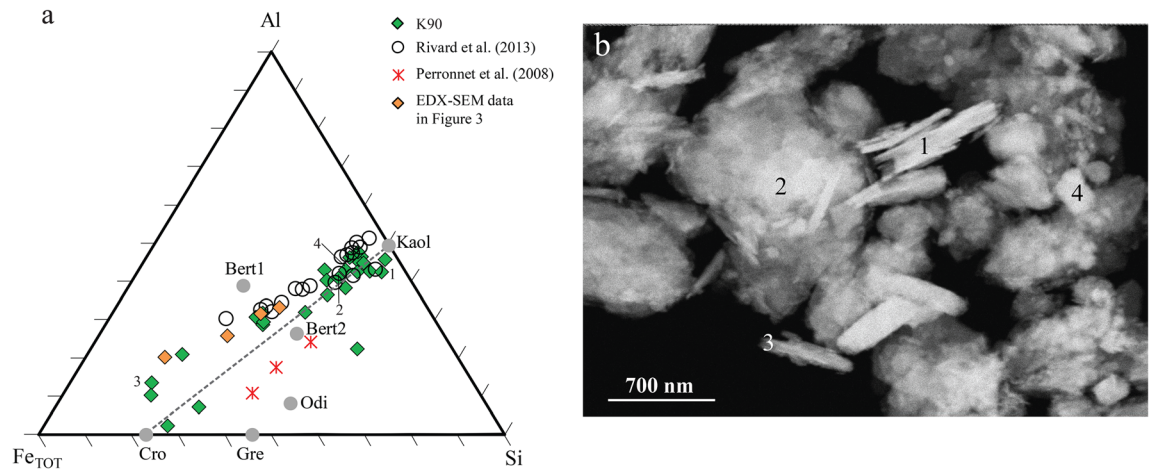

Fig. 4. **a** Al–Si–Fe_{tot} ternary diagrams of newly formed T–O phyllosilicates in the run product of kaolinite + Fe^0 experiment (K90). Their composition is compared with that of phyllosilicates synthesized by Rivard et al. (2013a) and Perronnet et al. (2008). The ideal trend (dashed gray line) indicating the compositional evolution from the dioctahedral pole of kaolinite toward the trioctahedral pole of cronstedtite is close to the experimental one. **b** STEM image of T–O phyllosilicates. Their TEM-EDX analyses indicated by numbers 1 to 4 are reported in the ternary diagram. Reference , indicated by gray circles, are: Kaol: kaolinite $Al_2Si_2O_5(OH)_4$; Gre: greenalite $(Fe^{2+}_{1.89}Fe^{3+}_{0.47}Mg_{0.32}\square_{0.31})Si_2O_5(OH)_4$ – Guggenheim et al. (1982); Bert1: berthierine $(Fe^{2+}_{1.49}Fe^{3+}_{0.22}Mg_{0.17}\square_{0.17})(Si_{1.15}Al_{0.85})O_5(OH)_4$; Bert2: berthierine $(Fe^{2+}_{1.01}Al_{0.82}Mg_{0.46}Fe^{3+}_{0.28}\square_{0.43})(Si_{1.74}Al_{0.26})O_5(OH)_4$ – Brindley (1982); Odi: odinite $(Fe^{3+}_{0.78}Mg_{0.77}Al_{0.56}Fe^{2+}_{0.28}Ti_{0.02}\ Mn_{0.01}\square_{0.58})(Si_{1.79}\ Al_{0.21})O_5(OH)_4$ – Bailey (1988); Cro: cronstedtite $(Fe^{2+}_{2.16}Fe^{3+}_{0.84})(Si_{1.16}\ Fe^{3+}_{0.84})O_5(OH)_4$ – Kogure et al. (2002)

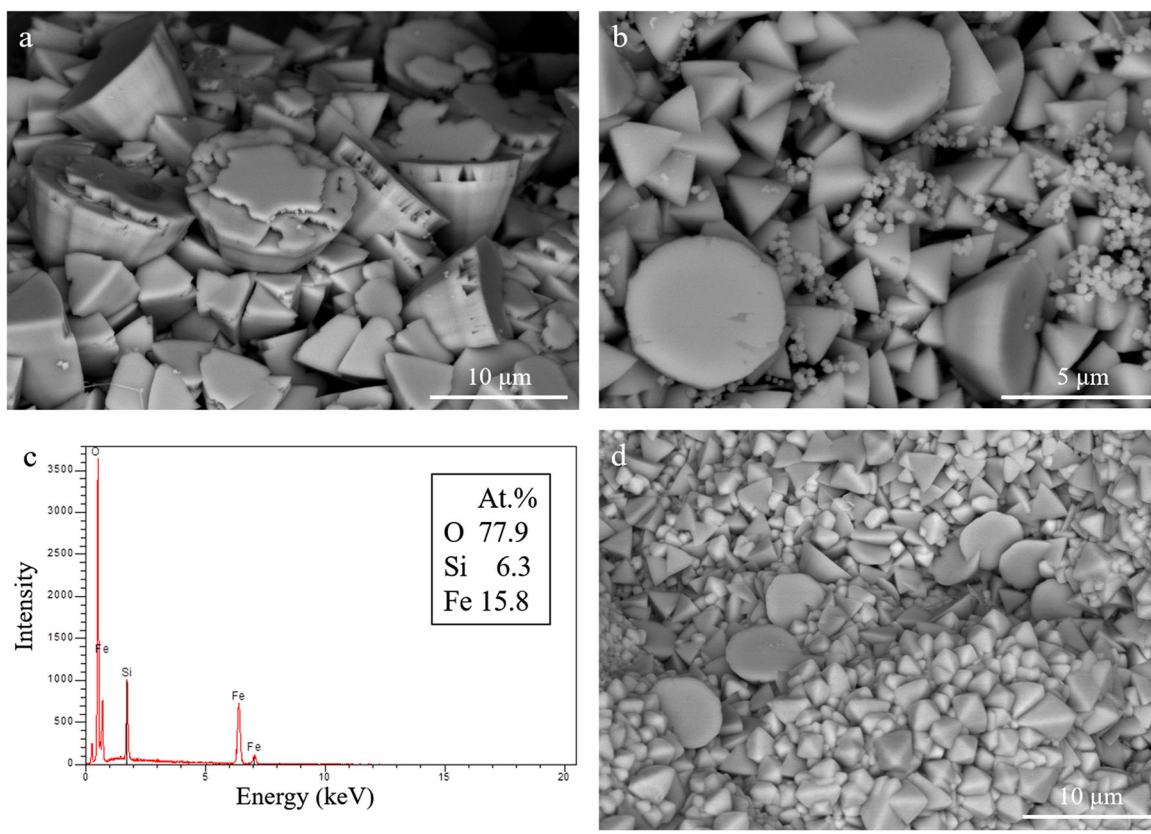

Fig. 5. **a**, **b** BSE-SEM images and **c** EDX data of cronstedtite in the experiment with Fontainebleau sandstone + Fe^0 at 90°C. They are characterized by a pyramidal morphology with triangular or pseudo-hexagonal cross sections. **d** BSE-SEM image of pyramidal and conical cronstedtites with magnetite crystals

https://doi.org/10.1007/s42860-020-00080-y Published online by Cambridge University Press

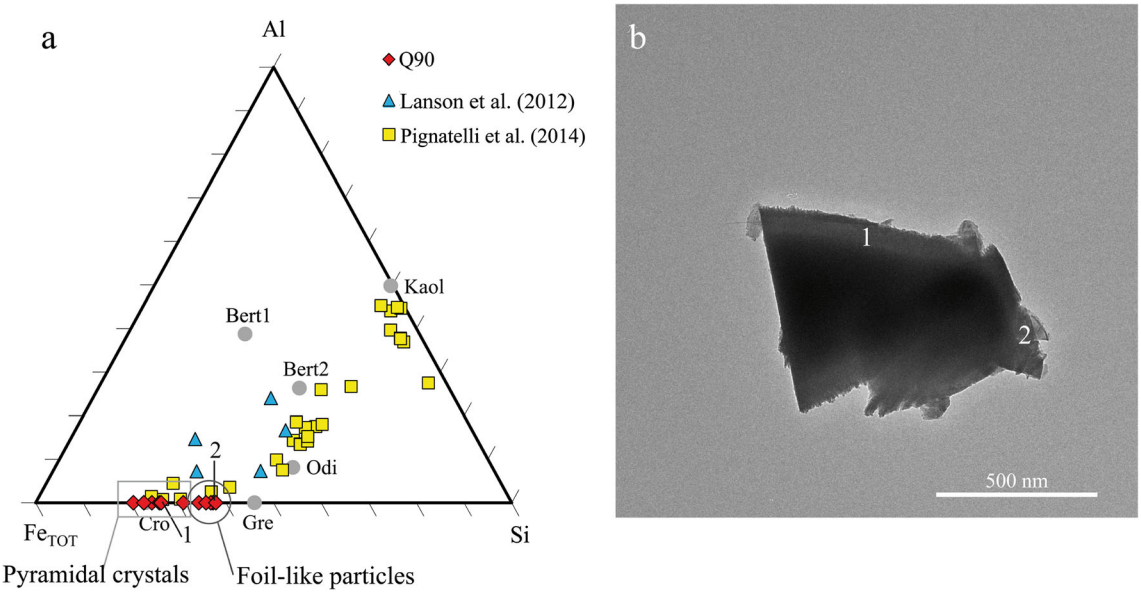

Fig. 6. a Al–Si–Fe_{tot} ternary diagram of newly formed T–O phyllosilicates in the run product of Fontainebleau sandstone + Fe^0 experiment (Q90). Reference are the same as in Fig. 4. **b** TEM image of cronstedtite observed in the Q90 run product

in the run product have compositions close to that of cronstedtite (Fig. 4). In a second run, greenalite was prevented from precipitating, implying the precipitation of cronstedtite together with Fe^{2+}-berthierine.

In order to understand why precipitation of magnetite and lepidocrocite were not predicted by the code, another simulation test was carried out by adding kaolinite gradually (10^{-4} moles/step for 39 steps) to mimic the reaction pathway. Lepidocrocite did not precipitate throughout the thermodynamic calculation. At the first step, iron is totally dissolved, magnetite, Fe^{2+}-berthierine, and cronstedtite form, and the pH reaches the value of 7.45. From the second step, the amount of cronstedtite increased slightly at the expense of magnetite, which dissolved completely when 0.0015 moles of kaolinite were dissolved ($pH_{90°C}$ = 7.25). At this point, the reaction ended because no source of iron was available form berthierine and cronstedtite (Fig. 10).

For experiment Q90, the list of minerals with a positive saturation index which may thus precipitate comprises of greenalite, cronstedtite, magnetite, lepidocrocite, ferrihydrite, and hematite. The last three were not observed in run products, thus they were ignored in further simulations. If both cronstedtite and greenalite are allowed to precipitate, cronstedtite never forms. Note (1) the greenalite formulae used in the database have the octahedral sites completely filled by Fe^{2+}, but greenalite can also contain Fe^{3+} (Guggenheim et al. 1982); (2) greenalite was not observed in the run product, whereas cronstedtite crystals were identified. For these reasons, greenalite was not allowed to precipitate in the subsequent simulation tests. The second simulation indicated that equilibrium was achieved when the amount of iron was completely consumed to form cronstedtite; the quartz was partially dissolved, but neither magnetite nor iron (oxyhydr)oxides were formed. Because cronstedtite was observed in association with magnetite in the run product, the hypothesis that the magnetite stability field decreases when the amount of Si in solution increases was tested. Thus, another simulation was carried out with a step-by-step addition of quartz (34 steps with increasing content of 0.0005 moles/step). The results indicated that both cronstedtite and magnetite formed and all of the iron was consumed in the first step. From the second step, the amount of cronstedtite increased at the expense of magnetite, which dissolved completely during the 5th step, i.e. when 0.0025 moles of quartz were added and consumed ($pH_{90°C}$ = 7.27 – Fig. 11a). At this point, the reaction was stopped. The addition of more quartz maked the solution in equilibrium with this mineral ([Si] = $8.97 \cdot 10^{-4}$ mol/kgw – Fig. 11b,c).

DISCUSSION

Kaolinite + Fe^0 Experiment (K90)

Fe-rich T–O phyllosilicates, magnetite, and lepidocrocite formed in the experiment with kaolinite and metal iron. Magnetite contains both Fe^{2+} and Fe^{3+}, whereas lepidocrocite contains only Fe^{3+} in its structure. Their formation indicates that iron oxidation occurred according to two reactions:

$$Fe^0 + 2H_2O \rightarrow Fe^{2+} + H_2 + 2OH^- \quad (1)$$

$$Fe^0 + 3H_2O \rightarrow Fe^{3+} + 3/2H_2 + 3OH^- \quad (2)$$

Both reactions produced OH^- and led to an increase in pH, favoring kaolinite dissolution. In fact, at temperatures closer to the experimental ones, the kaolinite dissolution rate was very low under near-neutral pH conditions (~$10^{-16.5}$ moles $cm^{-2}s^{-1}$ – rate based on Si release), but it will increase with pH (up to $10^{-14.4}$ moles $cm^{-2} \cdot s^{-1}$ at pH 12 – Carroll and Walther 1990).

https://doi.org/10.1007/s42860-020-00080-y Published online by Cambridge University Press

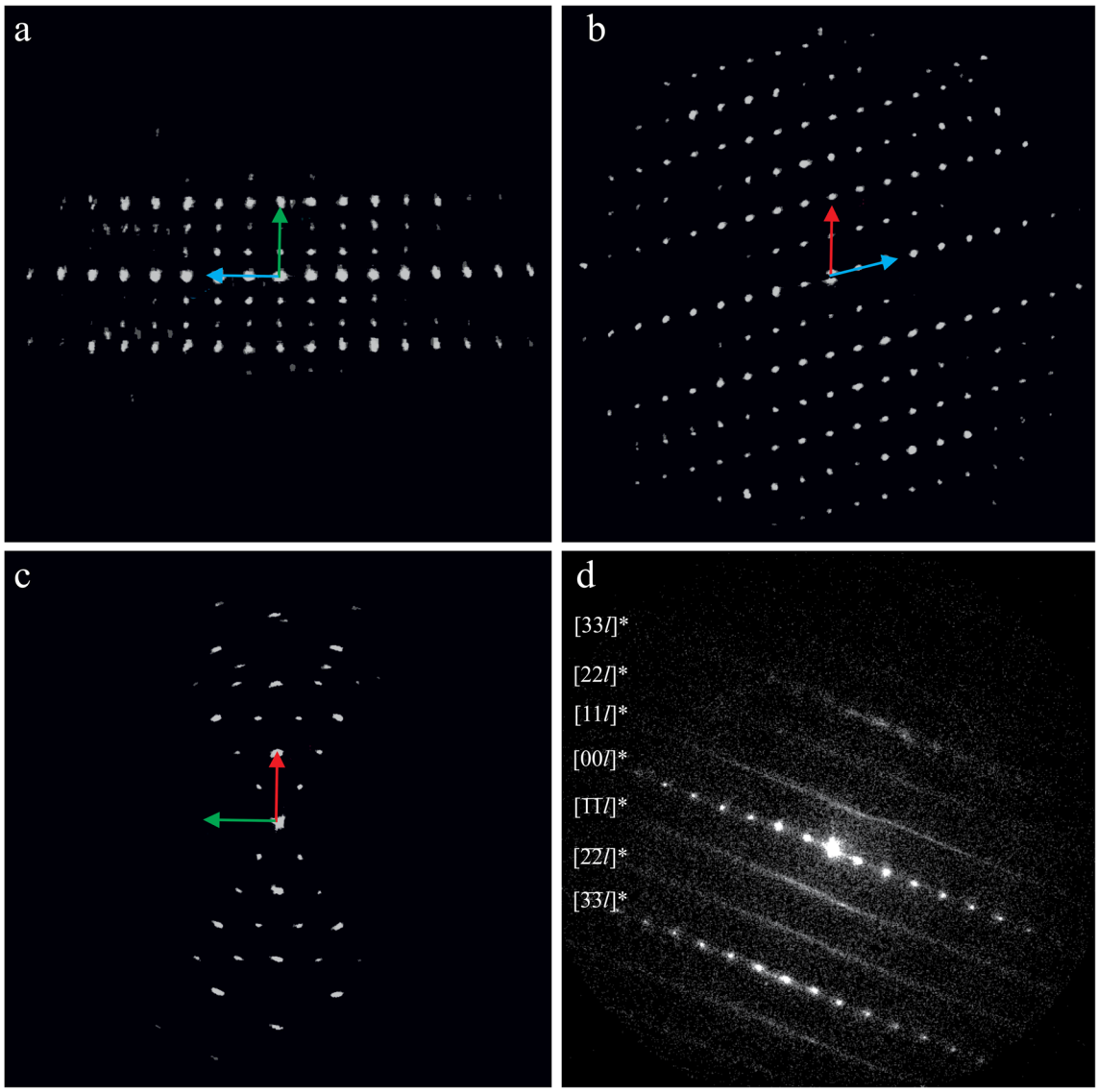

Fig. 7. Projection of 3D reconstructed diffraction volume from ED data of 1*M* cronstedtite polytype: **a** projection along *a**, **b** projection along *b**, **c** projection along *c**. **d** SAED pattern of (hhl_{hex})* plane for a disordered cronstedtite crystal. The projections of the main reciprocal axes are indicated: red vector: ***a****; green vector: ***b****; blue vector: ***c****

According to previous works on iron–clay interactions, the experimental conditions used here favored the formation of iron-rich T–O phyllosilicates, i.e. $T < 150°$ C, Fe/clays ≥ 0.33, Fe/liquid ≥ 10 (Perronnet et al. 2008; Mosser-Ruck et al. 2010; Rivard et al. 2013a). The composition of T–O phyllosilicates observed in the present work varied progressively from the kaolinite pole toward that of berthierine, although the most iron-rich phyllosilicates had a composition closer to that of cronstedtite (Fig. 4). This indicates both a progressive iron enrichment and a quasi-continuum evolution from a dioctahedral pole to a trioctahedral one.

The formation of Fe-bearing serpentines from kaolinite was reported in both natural environments and experimental syntheses. In nature, berthierine can form by interaction of kaolinite with a source of Fe, such as oolitic ironstones or Fe-bearing minerals such as siderite (Brindley 1951; Iijima and Matsumoto 1982; Bhattacharyya 1983). Under reducing conditions, the kaolinite transformation into greenalite is favored via cation substitutions in the octahedral sheet or a dissolution-recrystallization process (Giresse et al. 1988; Amouric et al. 1995).

In the laboratory, the hydrothermal synthesis of Fe-bearing serpentines from kaolinite showed the formation of berthierine-like minerals (Rivard et al. 2013a) or di-trioctahedral phases with composition between those of odinite and greenalite (Perronnet et al. 2008 – Fig. 4).

The composition of newly formed phyllosilicate particles with Fe < 40 at.% is similar to that reported by Rivard

https://doi.org/10.1007/s42860-020-00080-y Published online by Cambridge University Press

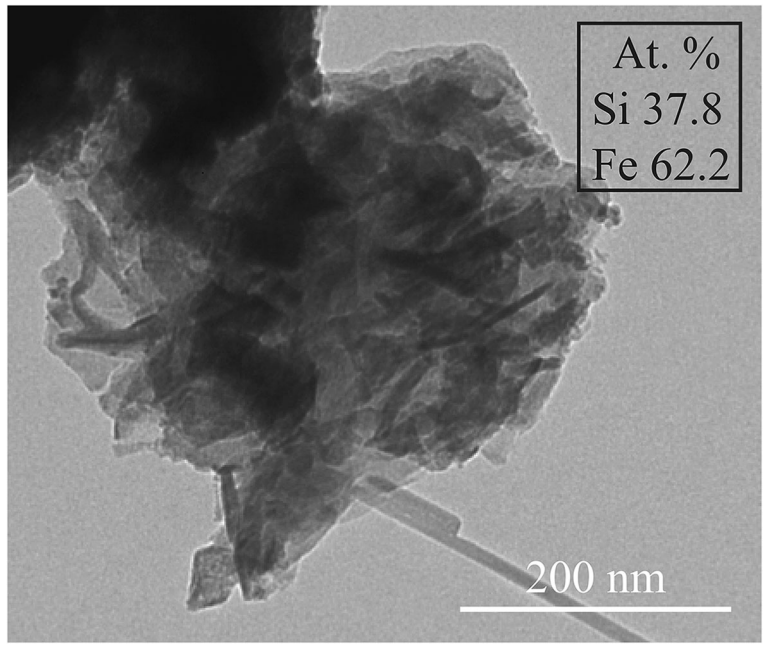

Fig. 8. TEM image of a Si-rich foil-like particle and its TEM-EDX data

et al. (2013a,b), but in the K90 experiment more Fe-rich particles also formed (Fig. 4). This difference was probably due probably to the experimental conditions. The temperature and the solution composition used by Rivard et al. (2013a,b) were the same as those used here, but they used a larger liquid/kaolinte ratio of 20 and a smaller Fe/

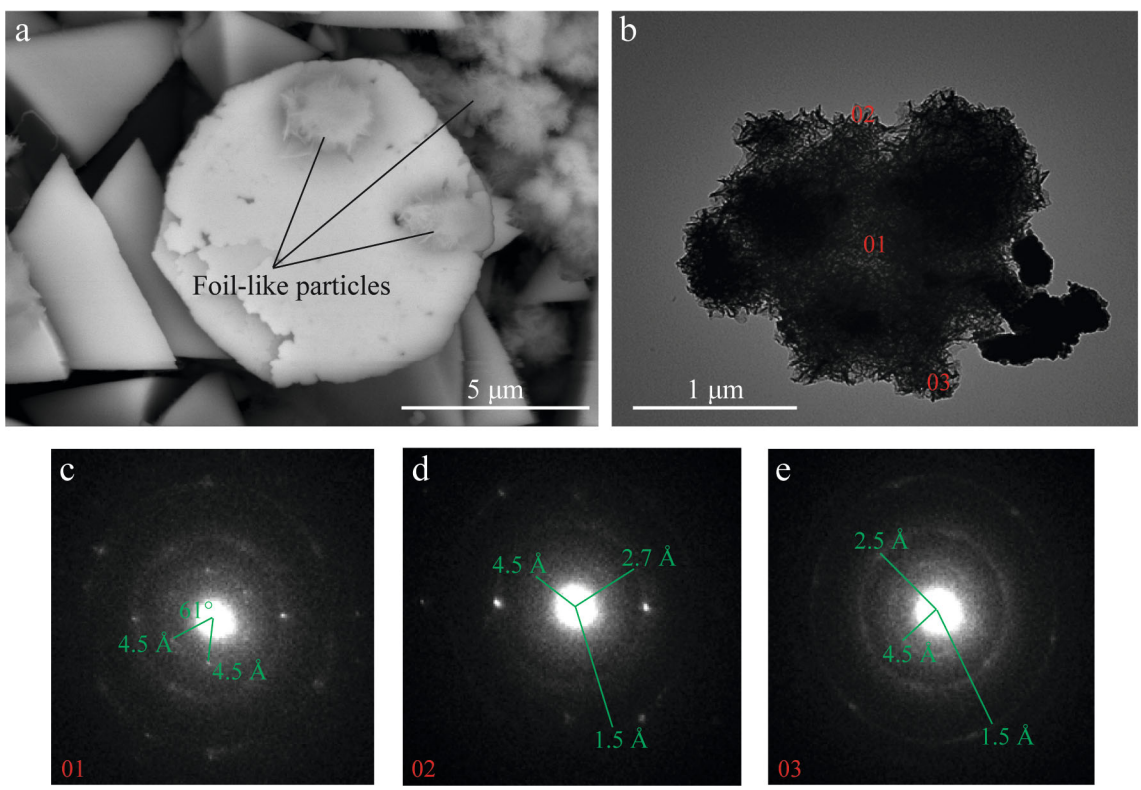

Fig. 9. a SEM image of foil-like particles on pyramidal crystals of cronstedtite. **b** TEM image of a foil-like particle. The latter is used to record SAED patterns in the zones 01, 02, and 03 (**c**, **d**, **e**)

https://doi.org/10.1007/s42860-020-00080-y Published online by Cambridge University Press

kaolinite mass ratio of 0.33. In addition, their experiment was run three times with different durations (1, 3, and 9 months) whereas the K90 experiment lasted only 75 days. Rivard et al. (2013a) observed no significant differences in the reaction product compositions of 1, 3, and 9 month experiments, and the evolution of the particles followed the same trend (Rivard et al. 2013a). Thus, the presence of more Fe-rich particles in the K90 experiment is probably related to the larger Fe/kaolinite mass ratio of 0.5.

The comparison of the run products with those of Perronnet et al. (2008) is more complicated because those authors did not use kaolinite as the starting material, but the FoCa7 bentonite which is composed of mixed-layer kaolinite-smectite (80 wt.%), kaolinite (4 wt.%), and other accessory minerals. The experimental conditions were quite different: temperature of 80°C, duration of 45 days, bentonite/solution mass ratio of 1/16.7, and Fe/bentonite ratio ranging from 0 to 0.33. These experimental conditions may explain why their particles showed a different compositional evolution.

Two possible mechanisms, not mutually exclusive, have been proposed to explain the kaolinite destabilization and berthierine formation: (1) epitaxial growth and (2) transformation kaolinite-berthierine through an intermediate phase called "protoberthierine."

(1) According to Rivard et al. (2013a), the TEM-EDX analyses of newly formed T–O phyllosilicates were spread between those of kaolinite and berthierine because they were mixtures of these two minerals with variable relative amounts. These authors suggested that pristine kaolinite dissolved preferentially on the edges and moderately on the basal faces and released Al and Si. These elements and Fe (dissolution of iron metal) present in solution allowed for the precipitation of berthierine layers on the basal faces of kaolinite, which acted as support for an epitaxial growth (Rivard et al. 2013a).

(2) Bhattacharyya (1983) described the progressive transformation of dioctahedral kaolinite to trioctahedral berthierine via an intermediate step leading to the formation of a "protoberthierine" as shown by the following reactions:

$$\underset{\text{Kaolinite}}{Al_2Si_2O_5(OH)_4} + 1.5Fe^{2+} \rightarrow \underset{\text{Protoberthierine}}{\left(Fe^{2+}{}_{1.5}\ Al\right)_{\Sigma=2.5}\ Si_2O_5(OH)_4} + Al^{3+} \quad (3)$$

$$\underset{\text{Protoberthierine}}{\left(Fe^{2+}{}_{1.5}\ Al\right)_{\Sigma=2.5}\ Si_2O_5(OH)_4} + Fe^{3+} + 0.5Fe^{2+} \rightarrow \underset{\text{Berthierine}}{\left(Fe^{2+}{}_2\ Fe^{3+}\right)_{\Sigma=3}\ (Si\ Al)_2O_5(OH)_4} + Si^{4+} \quad (4)$$

According to Bhattacharyya (1983), the variable Fe contents in newly formed T–O phases could be explained by different "degrees of structural degradation in kaolinite": the most degraded kaolinite is the most susceptible to the intake of iron.

Based on the experimental results of the current study, it was not possible to make a choice between these two mechanisms to explain the formation of berthierine in the run product. Epitaxial growth could not be confirmed because the SAED patterns of newly formed T–O phyllosilicates showed a superposition of two or more lattices. Whether the superposition corresponds to several crystals of the same T–O mineral or of a berthierine and kaolinite mixture cannot be established. Both berthierine grown epitaxially on kaolinite and the existence of protoberthierine would result in similar TEM-EDX data. On the assumption that protoberthierine could form, the kaolinite–berthierine transformation in this experiment can be described as follows:

$$\underset{\text{Kaolinite}}{Al_2Si_2O_5(OH)_4} + 0.6Fe^{2+} \rightarrow \underset{\text{Protoberthierine}}{\left(Al_{1.6}Fe^{2+}{}_{0.6}\right)_{\Sigma=2.2}\ Si_2O_5(OH)_4} + 0.4Al^{3+} \quad (5)$$

$$\underset{\text{Protoberthierine}}{\left(Al_{1.6}Fe^{2+}{}_{0.6}\right)_{\Sigma=2.2}\ Si_2O_5(OH)_4} + 1.7Fe^{2+} + 0.5Fe^{3+} \rightarrow \underset{\text{Berthierine}}{\left(Fe^{2+}{}_{2.3}\ Fe^{3+}{}_{0.5}Al_{0.2}\right)_{\Sigma=3}\ (Si_{1.3}\ Al_{0.7})_{\Sigma=2}O_5(OH)_4} + 0.7Al^{3+} + 0.7Si^{4+} \quad (6)$$

where the protoberthierine formula corresponds to the average TEM-EDX data with Fe at.% < 20% (Fig. 4), because berthierines usually have larger iron contents as shown in Fig. 12. Natural berthierines also contain variable amounts of Mg, unlike those analyzed here, because no Mg-bearing phase was found in the starting material used in this study. The berthierine formula was thus calculated from the average of the data with Fe at.% > 20% (Fig. 4), following the method of Brindley (1982), based on three octahedral sites and a total valence of cations equal to +14. The abundance of estimated Fe^{2+} is in agreement with the composition of natural samples and indicated that berthierine formed under reducing conditions (Brindley 1982; Iijima and Matsumoto 1982; Giresse et al. 1988; Hornibrook and Longstaffe 1996; Rivas-Sanchez et al. 2006).

The results of thermodynamic simulations highlight the transformation of kaolinite in Fe^{2+}-berthierine and Fe-richer serpentines compositionally close to cronstedtite, in agreement with the experimental observations.

Magnetite is also predicted to form, but not lepidocrocite. Two explanations are possible: (1) the calculations do not take into account kinetic factors that may influence the reaction pathway and the nature of end-products; and (2) experimental data indicated that lepidocrocite crystallizes only if the Si/Fe ratio in solution is <0.05 (Schwertmann and Thalmann 1976). As the presence of Si in solution prevents the formation of this hydroxide, it should form before the formation of serpentines.

https://doi.org/10.1007/s42860-020-00080-y Published online by Cambridge University Press

Knowing that lepidocrocite is an oxidation product of Fe^{2+} under neutral conditions (Liu et al. 2007), its formation during the cooling of the autoclave seems unlikely because the pH increases as the temperature decreases ($pH_{25°C}$ = 8.25). The simulations suggested that the equilibrium would be achieved when magnetite is dissolved, but in the run product it is still present. This means that at the end of the experiment, the system was probably not at equilibrium and a small Si content remained in the solution (Table 1, Fig. 10b).

Lepidocrocite can form in low chloride-containing solutions from a precursor, i.e. ferrihydrite or $Fe(OH)_2$ (Misawa et al. 1974; Schwertmann and Fechter 1994; Liu et al. 2007; de la Fuerte et al. 2016; Song et al. 2017). Ferrihydrite was not observed in the run product, but an unidentified Fe-bearing phase was found on the iron surface (Fig. 13). Based on the semi quantitative O/Fe ratio of ~4, this phase is thought not to be $Fe(OH)_2$ and could be a chloride green rust, which generally has an O/Fe ratio >2.5 (Refait et al. 1998). In this case, the lepidocrocite could have formed from a green rust which was an intermediate phase resulting from the easily oxidized $Fe(OH)_2$ (Refait and Génin 1997; Réguer et al. 2007).

Fontainebleau Sandstone + Fe^0 Experiment (Q90)

The iron oxidation reactions (1 and 2) release Fe^{2+} and Fe^{3+} into solution, favoring the formation of both magnetite and cronstedtite. The latter needs Si released by quartz dissolution to precipitate.

The formation of both magnetite and cronstedtite was also reported by Pignatelli et al. (2013, 2014) in a cooling experiment (90–40°C) simulating the interactions between iron and the Callovo-Oxfordian claystone of the Paris Basin. In addition to cronstedtite, greenalite and mixed-layered phases made of T–O–T and T–O phyllosilicates were also synthesized. These products had an intermediate composition between the starting clays and greenalite/cronstedtite (Fig. 6). This main difference could be due to claystone's complex mineralogical composition and the duration of experiments (6 months vs 75 days). In the experiment of Pignatelli et al. (2013, 2014), cronstedtite became unstable at $T \leq 50$°C and rare relict crystals remained at 40°C. These authors proposed that cronstedtite formed by precipitation from a supersaturated solution.

Iron T–O phyllosilicates with compositions close to cronstedtite and odinite were synthesized by Lantenois et al. (2005) and analyzed by Lanson et al. (2012) in order to investigate the interactions between dioctahedral smectites and iron at 80°C for 45 days (Fig. 6). Their newly formed phyllosilicates were richer in Si and Al than the cronstedtite crystals of this study and those of Pignatelli et al. (2013, 2014), and they had variable amounts of vacancies in the octahedral sheet (0.25 to 0.75 – Lanson et al. 2012).

In natural environments, cronstedtite has been observed in low-temperature hydrothermal systems and in carbonaceous chondrites (Frondel 1962; López-García et al. 1992; Rubin et al. 2007; Hybler et al. 2016, 2017), but very little information is available about the formation conditions (starting mineralogical mixture, pH, temperature, etc.), preventing comparison with the Q90 experiment. The investigations of chondrites confirms that cronstedtite formation is due to the iron and silicon released by oxidation of kamacite and dissolution of silicates (Tomeoka and Buseck 1985; Zolensky and McSween 1988). Pignatelli et al. (2017) recently showed that in chondrites, cronstedtite can form by pseudomorphic replacement of olivines and pyroxenes, in association with Fe-tochilinite and goethite. Considering the stability field of Fe-tochilinite and the presence of tochilinite/cronstedtite intergrowths, it follows that cronstedtite in chondrites formed at $T < 30$°C (Pignatelli et al. 2017). This is in agreement with thermodynamic simulations showing that the upper limit of cronstedtite stability is 100°C, whereas greenalite is stable up to 150°C (Schulte and Shock 2004; McAlister and Kettler 2008; Pignatelli et al. 2014).

From the structural point of view, sub-micrometric cronstedtite crystals investigated in this work by 3D ED belong to the 1*M* polytype or are characterized by a stacking disorder. Cronstedtite 1*M* polytype is quite rare in nature (Hybler et al. 2008), but 1*M* is commonly synthesized between 90 and 60°C. In this temperature range, other polytypes were obtained, such as $2M_1$ at 60–70°C and 3*A* at 80–90°C (Pignatelli et al. 2013; Hybler et al. 2018). The most abundant polytype in terrestrial and extraterrestrial samples is 1*T* (Müller et al. 1979; Zega and Buseck 2003; Hybler et al. 2008; Pignatelli et al. 2018), but this polytype seems difficult to reproduce in the laboratory; in fact, it was synthesized only once at 90°C in a mixed crystal with 1*M* (Hybler et al. 2018). Due to lack of knowledge, the differences in the polytypic sequence of synthetic and natural cronstedtite crystals cannot, currently, be explained.

Thermodynamic simulations give the reaction path describing the formation of cronstedtite and magnetite under the experimental conditions of the present study. The results indicate that iron is dissolved completely as well as magnetite, in disagreement with the experimental data where iron, magnetite, and cronstedtite coexist in the run product (Fig. 1b).

Table 1. Cation concentrations in run solutions measured by ICP-OES (given in both mg/L and mol/kgw to facilitate the comparison with thermodynamic simulation data). In the brackets, 1σ value was reported for each measurement

	$pH_{25°C}$	Al	Si	Fe	Units
K90	8.25	0.33 (0.10)	1.77 (0.18)	0.50 (0.10)	mg/L
		$1.2{\cdot}10^{-4}$	$6.3{\cdot}10^{-5}$	$8.9{\cdot}10^{-6}$	mol/kgw
Q90	7.38	0.16 (0.10)	6.15 (0.31)	8.46 (0.42)	mg/L
		$5.9{\cdot}10^{-6}$	$2.2{\cdot}10^{-4}$	$1.5{\cdot}10^{-4}$	mol/kgw

https://doi.org/10.1007/s42860-020-00080-y Published online by Cambridge University Press

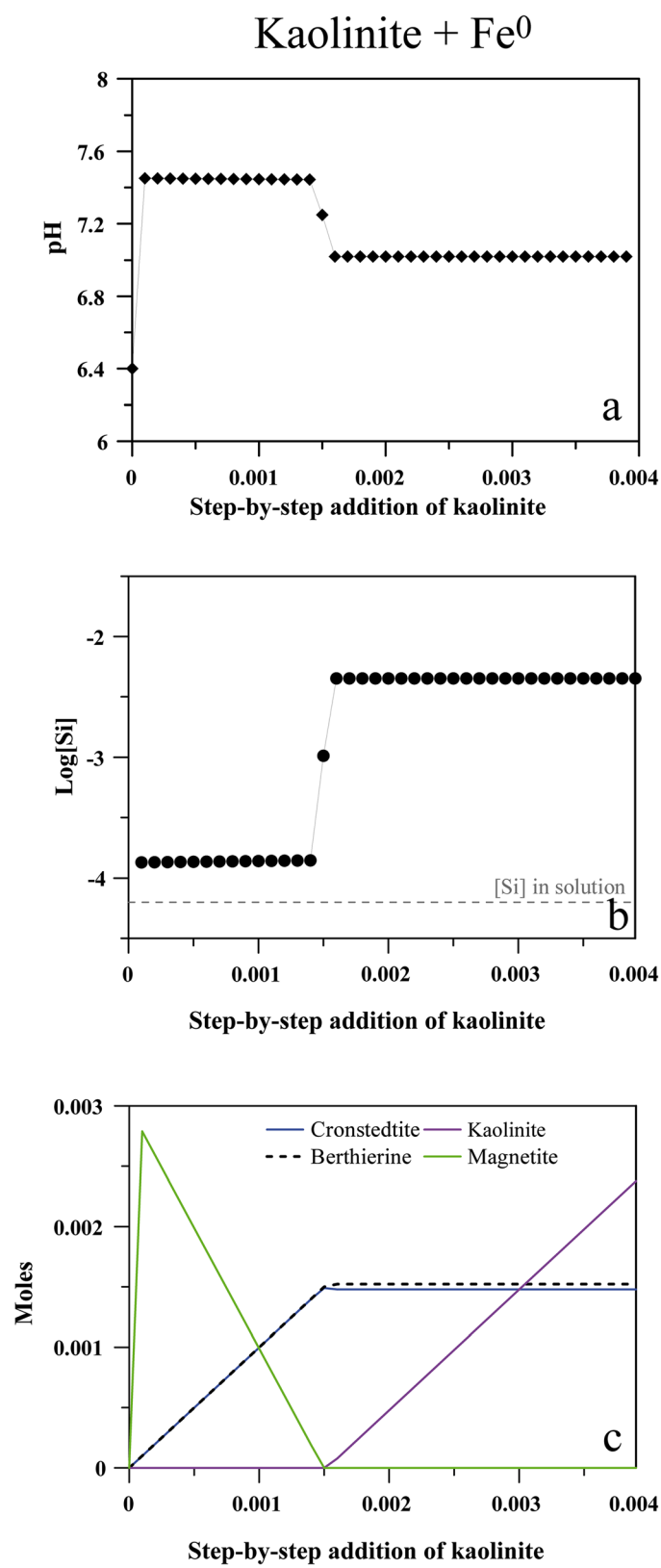

Fig. 10. Results of thermodynamic simulation for the experiment K90 obtained by a step-by-step addition of kaolinite (10^{-4} moles/step for 39 steps). **a** Evolution of pH, **b** Si concentration in solution, and **c** dissolution/precipitation of minerals. The dashed gray line indicates the Si content measured in the experimental solution

https://doi.org/10.1007/s42860-020-00080-y Published online by Cambridge University Press

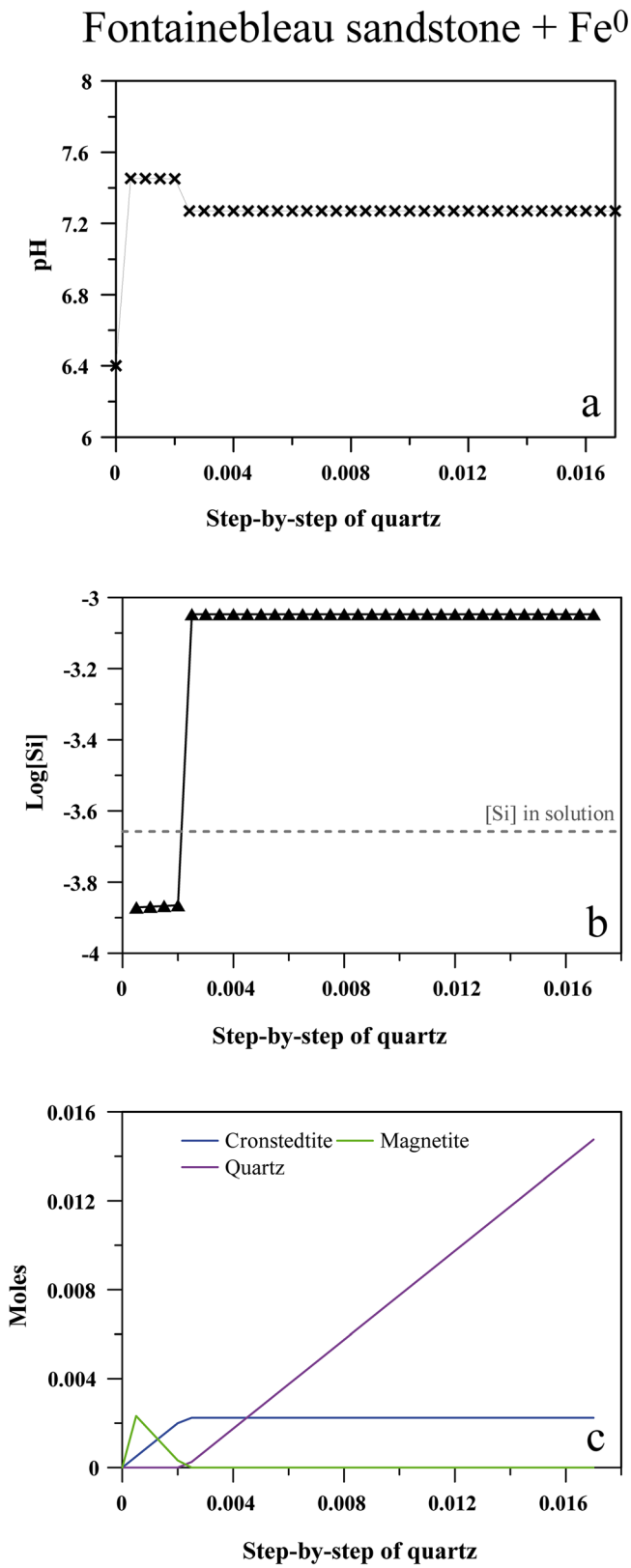

Fig. 11. Results of thermodynamic simulation for the experiment Q90 obtained by a step-by-step addition of quartz (0.0005 moles/step for 34 steps). **a** Evolution of pH, **b** Si concentration in solution, and **c** dissolution/precipitation of . The dashed gray line indicates the Si content measured in the experimental solution

https://doi.org/10.1007/s42860-020-00080-y Published online by Cambridge University Press

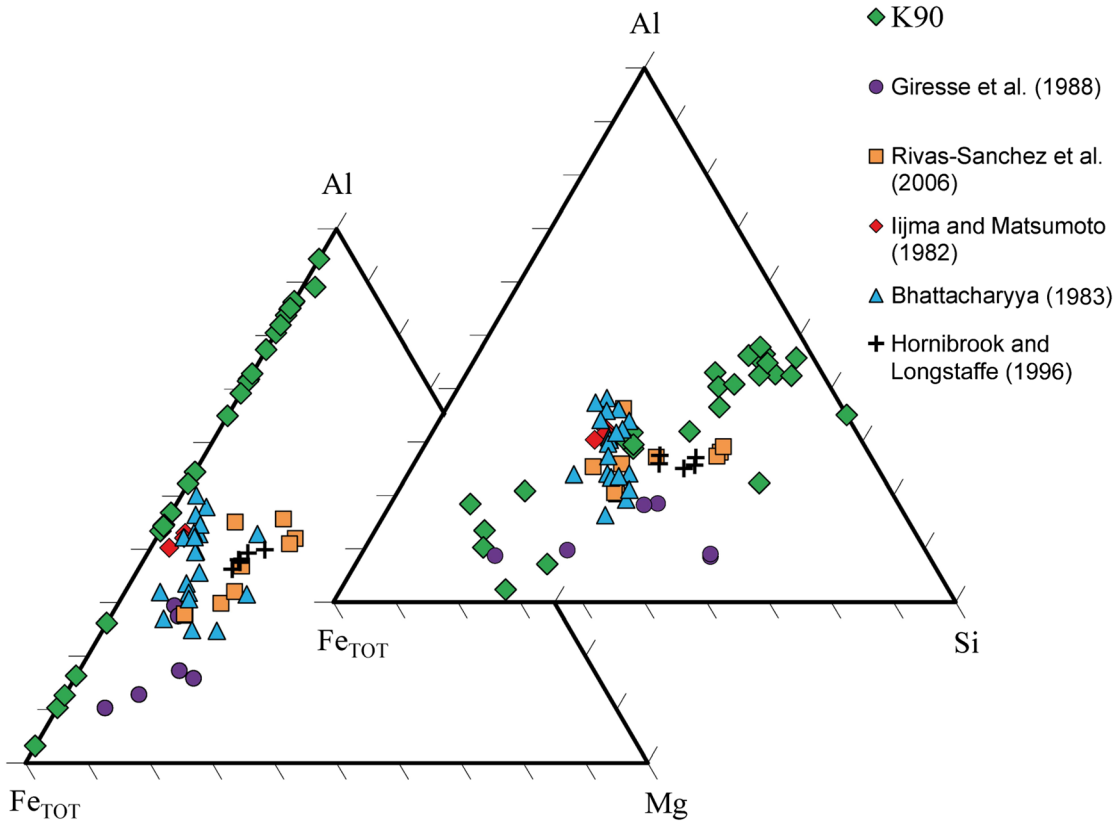

Fig. 12. Al–Si–Fe_{tot} and Al–Mg–Fe_{tot} ternary diagrams comparing the newly formed T–O phyllosilicates in experiment K90 and the compositions of natural berthierine crystals (Iijma and Matsumoto 1982; Giresse et al. 1988; Bhattacharyya 1983 and references therein; Hornibrook and Longstaffe 1996; Rivas-Sanchez et al. 2006)

Moreover, magnetite shows no sign of dissolution in SEM images. It follows that: (1) the reaction path probably did not come to the end in the Q90 experiment, probably because of short experimental duration (75 days), and/or the very slow dissolution rates of quartz and metal iron at 90°C under neutral pH ($1.57{\cdot}10^{-14}$ cm·s^{-1} and $9.12{\cdot}10^{-11}$ cm·s^{-1}, respectively (Van Lier et al. 1960; Schlegel et al. 2008); (2) modeling considers that all minerals dissolve and precipitate instantly when in reality they have different dissolution rates. Consequently, Fe would corrode much more quickly than quartz, and magnetite would then be the first mineral to form. After a further period of time, thanks to an increase in pH, quartz dissolution would provide silicon in solution, and the corrosion of the iron or a partial dissolution of the magnetite will release iron, favoring the precipitation of cronstedtite.

The experiment stopped probably at the third step of the simulation, where 0.0015 moles of quartz are dissolved and the $pH_{90°C}$ is 7.45 (Fig. 11a). At this step, the Si concentration released in solution is $1.36{\times}10^{-4}$ mol/kgw (Fig. 11b) which is very close to the concentration measured in the experimental solution ($2.2{\times}10^{-4}$ mol/kgw – Table 1). The difference of $0.84{\times}10^{-4}$ mol/kgw could be attributed to the dissolution of trace minerals present in the Fontainebleau sandstone, which is confirmed by the detection of Al in the run solution (Table 1).

CONCLUSIONS

For the first time, the effect of different starting mineralogical mixtures on the synthesis of Fe-bearing serpentines was shown. Two hydrothermal syntheses were carried out under the same conditions, with the exception of the Si source chosen, i.e. kaolinite and quartz (K90 and Q90 experiments, respectively). Although previous studies synthesized serpentines using gels or rocks (Dzene et al. 2018 and references therein), the aim of the current study was to underline the effects of composition and structure of the silicate precursors on newly formed serpentines. In addition, the Fe-serpentines synthesized here were well crystalline and have been characterized by several analytical techniques (XRD, SEM, TEM, and EDX).

The results have shown that different Fe-serpentines are formed in the K90 and Q90 experiments, i.e. berthierine from kaolinite and cronstedtite from quartz. Their growth mechanisms are also different; berthierine could form by epitaxial growth on kaolinite according to Rivard et al. (2013a), whereas cronstedtite forms probably by precipitation from a supersaturated solution (Pignatelli et al., 2013).

The formation of berthierine and cronstedtite in association with magnetite from their respective starting mineralogical mixtures was confirmed by the thermodynamic simulations.

https://doi.org/10.1007/s42860-020-00080-y Published online by Cambridge University Press

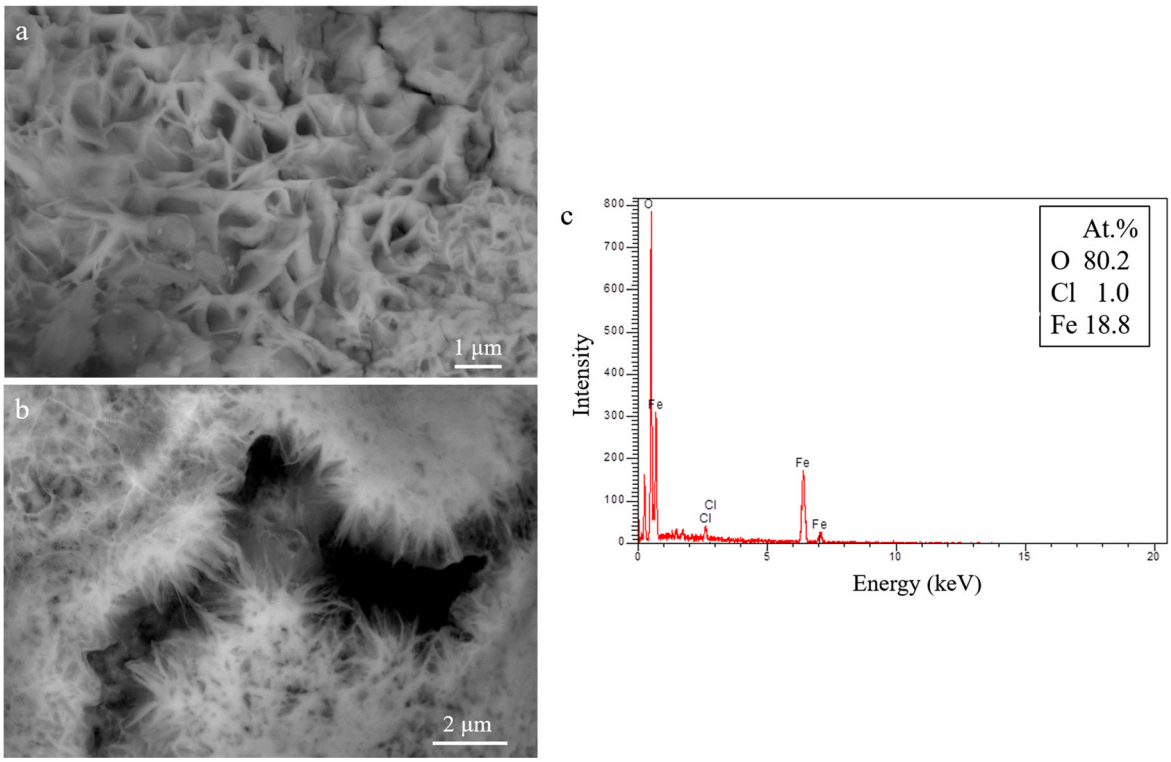

Fig. 13. **a**, **b** SEM images and **c** EDX spectrum of the Fe-bearing phase observed on the iron surface in experiment K90

The formation of these minerals needs Fe^{2+} and Fe^{3+} produced by previous oxidation of metal iron in the presence of water (see reactions 1 and 2). The oxidation produces H_2 and OH^-, leading to alkaline conditions and favoring the destabilization of kaolinite and quartz. The latter interact with Fe^{2+} and Fe^{3+} to form Fe-serpentines, according to:

$$Al_2Si_2O_5(OH)_4 + 3.3Fe^{2+} + 3.5Fe^{3+} + 10.7H_2O \rightarrow \quad (7)$$
$$\left(Fe^{2+}{}_{2.3}\ Fe^{3+}{}_{0.5}\ Al_{0.2}\right)_{\Sigma=3}\left(Si_{1.3}\ Al_{0.7}\right)_{\Sigma=2}O_5(OH)_4$$
$$+ 1.1Al(OH)_3 \ + 0.7SiO_2(aq) + 8.55H_2$$

$$3SiO_2 + +3.3Fe^{2+} + 3.4Fe^{3+} + 10.4H_2O \rightarrow \quad (8)$$
$$\left(Fe^{2+}{}_{2.3}\ Fe^{3+}{}_{0.7}\right)_{\Sigma=3}\left(Si_{1.3}\ Fe^{3+}{}_{0.7}\right)_{\Sigma=2}O_5(OH)_4 + 8.4H_2$$

Reactions 7 and 8 underline the importance of improving the current knowledge of Fe-serpentine formation due to the release of H_2, useful for several industrial purposes and sustainable energy (Ramachandran and Menon 1998; Edwards et al. 2007). In addition, H_2 generation is a key point to be investigated further with the aim of clarifying the possible relationship between Fe-serpentines and the origin of life (McCollom and Seewald 2013).

H_2 production during Fe-serpentine formation should be studied and quantified by performing more experiments using autoclaves equipped with *P-T* probes for in situ monitoring, as has been done for other minerals (e.g. Bourdelle et al. 2014, 2017). The new syntheses will also allow for (1) testing of the effect of other physical-chemical parameters (temperature, iron/silicate ratio, solution composition, etc.) on Fe-serpentines formation (2) a greater quantity of Fe-serpentines to be obtained in order to determine how their thermodynamic parameters vary as a function of their composition and polytypic sequence and, thus, improve the current geochemical databases. The shortcomings in our understanding of the thermodynamics of Fe-serpentines could be the source of inconsistencies between the experimental and thermodynamic results, and of inaccurate predictions for their formation and long-term stability (Seyfried et al. 2007; Pignatelli et al. 2014; Dzene et al. 2018). (3) It may also allow the determination of precipitation and dissolution rates of Fe-serpentines to improve the prediction of geochemical modeling.

ACKNOWLEDGMENTS

The authors thank Dr Iryna Andrusenko for helping in the acquisition and analysis of electron diffraction data. Authors Mauro Gemmi and Enrico Mugnaioli were supported by Regione Toscana through the FELIX project (Por CREO FESR 2014-2020 action). Prof. Fernando Nieto, two anonymous reviewers, and the Editor-in-Chief, Prof. Joseph W. Stucki, are also thanked for their corrections and suggestions which helped to improve the final version of the manuscript.

Compliance with ethical standards

Conflict of Interest

https://doi.org/10.1007/s42860-020-00080-y Published online by Cambridge University Press

The authors declare that they have no conflict of interest.

Funding

Funding sources are as stated in the acknowledgments.

REFERENCES

Amouric, M., Parron, C., Casalini, L., & Giresse, P. (1995). A (1:1) 7-Å Fe phase and its transformation in recent sediments: an HRTEM and AEM study. *Clays and Clay Minerals, 43*, 446–454.

Bailey, S. W. (1969). Polytypism of trioctahedral 1:1 layer silicates. *Clays and Clay Minerals, 17*, 355–371.

Bailey, S. W. (1988). Odinite, a new dioctahedral-trioctahedral Fe^{3+}-rich 1:1 clay mineral. *Clay Minerals, 23*, 237–247.

Barber, D. J. (1981). Matrix phyllosilicates and associated minerals in C2M carbonaceous chondrites. *Geochimica et Cosmochimica Acta, 45*, 945–970.

Bhattacharyya, D. P. (1983). Origin of berthierine in ironstones. *Clays and Clay Minerals, 31*, 173–182.

Bildstein, O., Trotignon, L., Perronnet, M., & Jullien, M. (2006). Modelling iron–clay interactions in deep geological disposal conditions. *Physics and Chemistry of the Earth, 31*, 618–625.

Bourdelle, F., Truche, L., Pignatelli, I., Mosser-Ruck, R., Lorgeoux, C., Roszypal, C., & Michau, N. (2014). Iron–clay interactions under hydrothermal conditions: impact of specific surface area of metallic iron on reaction pathway. *Chemical Geology, 381*, 194–205.

Bourdelle, F., Mosser-Ruck, R., Truche, L., Lorgeoux, C., Pignatelli, I., & Michau, N. (2017). A new view on iron-claystone interactions under hydrothermal conditions (90°C) by monitoring in situ pH and H_2 generation. *Chemical Geology, 466*, 600–607.

Brindley, G. W. (1951). The crystal structures of some chamosite minerals. *Mineralogical Magazine, 29*, 502–525.

Brindley, G. W. (1982). Chemical compositions of berthierines – A review. *Clays and Clay Minerals, 30*, 153–155.

Browning, L. B., McSween Jr., H. Y., & Zolensky, M. E. (1996). Correlated alteration effects in CM carbonaceous chondrites. *Geochimica et Cosmochimica Acta, 60*, 2621–2633.

Calvin, W. M. (1998). Could Mars be dark and altered? *Geophysical Research Letters, 25*, 1597–1600.

Calvin, W. M., & King, T. V. V. (1997). Spectral characteristics of iron-bearing phyllosilicates: Comparison to Orgueil (CI1), and Murchison and Murray (CM2). *Meteoritics & Planetary Science, 32*, 693–701.

Carroll, S. A., & Walther, J. V. (1990). Kaolinite dissolution at 25°, 60°, and 80°C. *American Journal of Science, 290*, 797–810.

Changela, H. G., & Bridges, J. C. (2011). Alteration assemblages in the nakhlites: variation with depth on Mars. *Meteoritics & Planetary Science, 45*, 1847–1867.

Cliff, G., & Lorimer, G. W. (1975). The quantitative analysis of thin specimen. *Journal of Microscopy, 103*, 203–207.

Cudennec, Y., & Lecerf, A. (2006). The transformation of ferrihydrite into goethite or hematite, revisited. *Journal of Solid State Chemistry, 179*, 716–722.

de Combarieu, G., Schlegel, M. L., Neff, D., Foy, E., Vantelon, D., Barboux, P., & Gin, S. (2011). Glass-iron-clay interactions in a radioactive waste geological disposal: An integrated laboratory-scale experiment. *Applied Geochemistry, 26*, 65–79.

de la Fuerte, D., Díaz, I., Alcántara, J., Chico, B., Simancas, J., Llorente, I., García-Delgado, A., Jiménez, J. A., Adeva, P., & Morcillo, M. (2016). Corrosion mechanisms of mild stell in chloride-rich atmospheres. *Materials and Corrosion, 67*, 227–238.

Dove, P. M., & Crerar, D. A. (1990). Kinetics of quartz dissolution in electrolyte solutions using a hydrothermal mixed flow reactor. *Geochimica et Cosmochimica Acta, 54*, 955–969.

Dove, P., & Elston, S. F. (1992). Dissolution kinetics of quartz in sodium chloride solutions: analysis of existing data and a rate model for 25°C. *Geochimica et Cosmochimica Acta, 56*, 4147–4156.

Dove, P. M., Han, N., & De Yoreo, J. J. (2005). Mechanisms of classical crystal growth theory explain quartz and silicate dissolution behavior. *Proceedings of the National Academy of Sciences, 102*, 15357–15363.

Ďurovič, S. (1997). Cronstedtite-1*M* and co-existence of 1*M* and 3*T* polytypes. *Ceramics-Silikáty, 41*, 98–104.

Dzene, L., Brendlé, J., Limousy, L., Dutournié, P., Martin, C., & Michau, N. (2018). Synthesis of iron-rich tri-octahedral clay minerals: a review. *Applied Clay Science, 166*, 276–287.

Edwards, P. P., Kuznetsov, V. L., & David, W. I. F. (2007). Hydrogen energy. *Philosophical Transactions of the Royal Society, 365*, 1043–1056.

Elmaleh, A., Tarantino, S. C., Zema, M., Devouard, B., & Fialin, M. (2012). The low-temperature magnetic signature of Fe-rich serpentine in CM2 chondrites: comparison with terrestrial cronstedtite and evolution with the degree of alteration. *Geochemistry Geophysics Geosystems, 13*, Q05Z42. https://doi.org/10.1029/2011GC003964.

Elmaleh, A., Bourdelle, F., Caste, F., Benzerara, K., Leroux, H., & Devouard, B. (2015). Formation and transformations of Fe-rich serpentines by asteroidal aqueous. *Geochimica et Cosmochimica Acta, 158*, 162–178.

Frondel, C. (1962). Polytypism in cronstedtite. *American Mineralogist, 47*, 781–783.

Geiger, C. A., Henry, D. L., Bailey, S. W., & Maj, J. J. (1983). Crystal structure of cronstedtite-2H_2. *Clays and Clay Minerals, 31*, 97–108.

Gemmi, M., Mugnaioli, E., Gorelik, T. E., Kolb, U., Palatinus, L., Boullay, P., Hovmöller, S., & Abrahams, J. P. (2019). 3D Electron Diffraction: the nanocrystallography revolution. *ACS Central Science, 5*, 1315–1329.

Giresse, P., Wiewiora, A., & Lacka, B. (1988). Mineral phases and processes within green peloids from two recent deposits near the Congo river mouth. *Clay Minerals, 23*, 447–458.

Gole, M. L. (1980a). Low-temperature retrograde minerals in metamorphosed Archean banded iron-formations, Western Australia. *The Canadian Mineralogist, 18*, 205–214.

Gole, M. J. (1980b). Mineralogy and petrology of very-low metamorphic grade Archean banded iron-formations, Weld Range, Western Australia. *American Mineralogist, 65*, 8–25.

Guggenheim, S., Bailey, S. W., Eggleton, R. A., & Wilkes, P. (1982). Structural aspects of greenalite and related minerals. *The Canadian Mineralogist, 20*, 1–18.

Guillaume, D., Neaman, A., Cathelineau, M., Mosser-Ruck, R., Peiffert, C., Abdelmoula, M., Dubessy, J., Villiéras, F., Baronnet, A., & Michau, N. (2003). Experimental synthesis of chlorite from smectite at 300°C in the presence of metallic Fe. *Clay Minerals, 38*, 281–302.

Hicks, L. J., Bridges, J. C., & Gurman, S. J. (2014). Ferric saponite and serpentine in the nakhlite martian meteorites. *Geochimica et Cosmochimica Acta, 136*, 194–210.

Hornibrook, E. R. C., & Longstaffe, F. J. (1996). Berthierines from the Lower Cretaceous Clearwater formation, Alberta, Canada. *Clays and Clay Minerals, 44*, 1–21.

Hybler, J. (2014). Refinement of cronstedtite-1*M*. *Acta Crystallographica, B70*, 963–972.

Hybler, J., Petříček, V., Ďurovič, S., & Smrčok, L. (2000). Refinement of the crystal structure of cronstedtite-1*T*. *Clays and Clay Minerals, 48*, 331–338.

Hybler, J., Petříček, V., Fábry, J., & Ďurovič, S. (2002). Refinement of the crystal structure of cronstedtite-2*H*2. *Clays and Clay Minerals, 50*, 601–613.

Hybler, J., Ďurovič, S., & Kogure, T. (2008). Polytypism in cronstedtite. *Acta Crystallographica, A64*, 498–499.

Hybler, J., Sejkora, J., & Venclík, V. (2016). Polytypism of cronstedtite from Pohled, Czech Republic. *European Journal of Mineralogy, 28*, 765–775.

Hybler, J., Števko, M., & Sejkora, J. (2017). Polytypism of cronstedtite from Nižná Slaná, Slovakia. *European Journal of Mineralogy, 29*, 91–99.

Hybler, J., Klementová, M., Jarošová, M., Pignatelli, I., Mosser-Ruck, R., & Ďurovič, S. (2018). Polytype identification in trioctahedral 1:1 layer silicates. *Clays and Clay Minerals, 66*, 379–402.

Iijima, A., & Matsumoto, R. (1982). Berthierine and chamosite in coal measures of Japan. *Clays and Clay Minerals, 30*, 264–274.

Kogure, T., Hybler, J., & Yoshida, H. (2002). Coexistence of two polytypic groups in cronstedtite from Lostwithiel England. *Clays and Clay Minerals, 50*, 504–513.

Kolb, U., Mugnaioli, E., & Gorelik, T. E. (2011). Automated electron diffraction tomography – a new tool for nanocrystal structure analysis. *Crystal Research and Technology, 46*, 542–554.

Kreutzer, S., Friedrich, J., Sanderson, D., Adamiec, G., Chruśscińska, A., Fasoli, M., Martini, M., Polymeris, G. S., Burbidge, C. I., & Schmidt, C. (2017). Les sables de Fontainebleau: a natural quartz reference sample and its characterization. *Ancient TL, 35*, 21–31.

Lanson, B. (1997). Decomposition of experimental X-ray diffraction patterns (profile fitting): a convenient way to study clay minerals. *Clays and Clay Minerals, 45*, 132–146.

Lanson, B., & Besson, G. (1992). Characterisation of the end of smectite-to-illite transformation: decomposition of X-ray patterns. *Clays and Clay Minerals, 40*, 40–52.

Lanson, B., Van Lantenois, S., Aken, P. A., Bauer, A., & Plançon, A. (2012). Experimental investigation of smectite interaction with metal iron at 80°C: structural characterization of newly formed Fe-rich phyllosilicates. *American Mineralogist, 97*, 864–871.

Lantenois, S., Lanson, B., Muller, F., Bauer, A., Jullien, M., & Plançon, A. (2005). Experimental study of smectite interaction with metal Fe at low temperature: 1. Smectite destabilization. *Clays and Clay Minerals, 53*, 597–612.

Lauretta, D. S., Hua, X., & Buseck, P. R. (2000). Mineralogy of fine-grained rims in the ALH 81002 CM chondrite. *Geochimica et Cosmochimica Acta, 64*, 3263–3273.

Lee, M. R., & Chatzitheodoris, E. (2016). Replacement of glass in the Nakhla meteorite by berthierine: implications for understanding the origins of aluminum-rich phyllosilicates on Mars. *Meteoritics & Planetary Science, 51*, 1643–1653.

Liu, H., Li, P., Zhu, M., Wei, Y., & Sun, Y. (2007). Fe(II)-induced transformation from ferrihyfrite to lepidocrocite and goethite. *Journal of Solid State Chemistry, 180*, 2121–2128.

López-García, J. A., Manteca, J. I., Prieto, A. C., & Calvo, B. (1992). Primera aparicíon en España de cronstedtita. Caracterizacíon estructural. *Boletín de la Sociedad Española de Mineralogía, 15*, 21–25.

McAlister, J. A., & Kettler, R. M. (2008). Metastable equilibria among dicarboxylic acids and oxidation state during aqueous alteration on the CM2 chondrite parent body. *Geochimica et Cosmochimica Acta, 72*, 233–241.

McCollom, T. M., & Seewald, J. S. (2013). Serpentinites, hydrogen, and life. *Elements, 9*, 129–134.

Misawa, T., Hashimoto, K., & Shimodaira, S. (1974). The mechanism of formation of iron oxide and oxyhydroxides in aqueous solutions at room temperature. *Corrosion Science, 14*, 131–149.

Mosser-Ruck, R., Cathelineau, M., Guillaume, D., & Charpentier, D. (2010). Effects of temperature, pH, and iron/clay and liquid/clay ratios on experimental conversion of dioctahedral smectite to berthierine, chlorite, vermiculite, or saponite. *Clays and Clay Minerals, 58*, 280–291.

Mugnaioli, E., & Gemmi, M. (2018). Single-crystal analysis of nanodomains by electron diffraction tomography: mineralogy at the order-disorder borderline. *Zeitschrift für Kristallographie, 233*, 163–178.

Müller, W. F., Kurat, G., & Kracher, A. (1979). Chemical and crystallographic study of cronstedtite in the matrix of the Cochabamba (CM2) carbonaceous chondrite. *Tschermaks Mineralogische und Petrographische Mitteilungen, 26*, 293–304.

Parkhurst, D. & Appelo, C.A.J. (1999). *User's guide to PHREEQC (version 2) - a computer program for speciation, reaction-path, 1D-transport, and inverse geochemical calculations*. U.S. Geological Survey Water Resources Investigation Report 99, 99-4259. U.S. Geological Survey, Reston, Virginia, USA. 312 pp.

Perronnet, M., Jullien, M., Villiéras, F., Raynal, J., Bonnin, D., & Bruno, G. (2008). Evidence of a critical content in Fe(0) on FoCa7 bentonite reactivity at 80°C. *Applied Clay Science, 38*, 187–202.

Pignatelli, I., Mugnaioli, E., Hybler, J., Mosser-Ruck, R., Cathelineau, M., & Michau, N. (2013). A multi-technique characterization of cronstedtite synthesized by iron-clay interaction in a step-by-step cooling procedure. *Clays and Clay Minerals, 61*, 277–289.

Pignatelli, I., Bourdelle, F., Bartier, D., Mosser-Ruck, R., Truche, L., Mugnaioli, E., & Michau, N. (2014). Iron-clay interactions: detailed study of the mineralogical transformation of claystone with emphasis on the formation of iron-rich T-O phyllosilicates in a step-by-step cooling experiment from 90°C to 40°C. *Chemical Geology, 387*, 1–11.

Pignatelli, I., Marrocchi, Y., Vacher, L., Delon, R., & Gounelle, M. (2016). Multiple precursors of secondary mineralogical assemblages in CM chondrites. *Meteoritics & Planetary Science, 51*, 785–805.

Pignatelli, I., Marrocchi, Y., Mugnaioli, E., Bourdelle, F., & Gounelle, M. (2017). Mineralogical, crystallographic and redox features of the earliest stages of fluid alteration in CM chondrites. *Geochimica et Cosmochimica Acta, 209*, 106–122.

Pignatelli, I., Mugnaioli, E., & Marrocchi, Y. (2018). Cronstedtite polytypes in the Paris meteorite. *European Journal of Mineralogy, 30*, 349–354.

Ramachandran, R., & Menon, R. K. (1998). An overview of industrial uses of hydrogen. *International Journal of Hydrogen Energy, 23*, 593–598.

Refait, P., & Génin, J. M. R. (1997). The mechanisms of oxidation of ferrous hydroxychloride β-$Fe_2(OH)_3Cl$ in aqueous solution: the formation of akaganeite vs goethite. *Corrosion Science, 39*, 539–553.

Refait, P., Abdelmoula, M., & Génin, J. M. R. (1998). Mechanisms of formation and structure of green rust one in aqueous corrosion of iron in the presence of chloride ions. *Corrosion Science, 40*, 1547–1560.

Réguer, S., Dillmann, P., & Mirambet, F. (2007). Buried iron archeological artefacts: corrosion mechanisms related to the presence of Cl-containing phases. *Corrosion Science, 49*, 2726–2744.

Rivard, C., Pelletier, M., Michau, N., Razafitianamaharavo, A., Bihannic, I., Abdelmoula, M., Ghanbaja, J., & Villiéras, F. (2013a). Berthierine-like mineral formation and stability during the interaction of kaolinite with metallic iron at 90°C under anoxic and oxic conditions. *American Mineralogist, 98*, 163–180.

Rivard, C., Montargès-Pelletier, E., Vantelon, D., Pelletier, M., Karunakaran, C., Mochot, L. J., Villieras, F., & Michau, N. (2013b). Combination of multi-scale and multi-edge X-ray spectroscopy for investigating the products obtained from the interaction between kaolinite and metallic iron in anoxic conditions at 90°C. *Physics and Chemistry of Minerals, 40*, 115–132.

Rivas-Sanchez, M. L., Alva-Valdivia, L. M., Arenas-Alatorre, J., Urrutia-Fucugauchi, J., Ruiz-Sandoval, M., & Ramos-Molina, M. A. (2006). Berthierine and chamosite hydrothermal: genetic guides in the Peña Colorada magnetite-bearing ore deposit, Mexico. *Earth Planets and Space, 58*, 1389–1400.

Rubin, A. E., Trigo-Rodríguez, J. M., Huber, H., & Wasson, J. T. (2007). Progressive aqueous alteration of CM carbonaceous chondrites. *Geochimica et Cosmochimica Acta, 71*, 2361–2382.

Saadi, F. A., Wolf, K.-H., & Kruijsdijk, C. (2017). Characterization of Fontainebleau sandstone: quartz overgrowth and its impact on pore-throat framework. *Journal of Petroleum & Environmental Biotechnology, 8*, 1–12.

Schlegel, M. L., Bataillon, C., Benhamida, K., Blanc, C., Menut, D., & Lacour, J. L. (2008). Metal corrosion and argillite transformation at the water-saturated, high-temperature iron-clay interface: a microscopic-scale study. *Applied Geochemistry, 23*, 2619–2633.

Schulte, M., & Shock, E. (2004). Coupled organic synthesis and mineral alteration on the meteorite parent bodies. *Meteoritics & Planetary Science, 46*, 1577–1590.

Schwertmann, U., & Fechter, H. (1994). The formation of green rust and its transformation to lepidocrocite. *Clay Minerals, 29*, 87–92.

Schwertmann, U., & Thalmann, H. (1976). The influence of [Fe(II)], [Si], and pH on the formation of lepidocrocite and ferrihydrite

during oxidation of aqueous $FeCl_2$ solutions. *Clay Minerals, 11*, 189–200.

Seyfried Jr., W. E., Foustoukos, D. I., & Fu, Q. (2007). Redox evolution and mass transfer during serpentinization: An experimental and theoretical study at 200°C, 500 bar with implications for ultramafic-hosted hydrothermal systems at Mid-Ocean Ridges. *Geochimica et Cosmochimica Acta, 71*, 3872–3886.

Smrčok, L., & Weiss, Z. (1993). DIFK91: a program for the modelling of powder diffraction patterns on a PC. *Journal of Applied Crystallography, 26*, 140–141.

Smrčok, L., Ďurovič, S., Petříček, V., & Weiss, Z. (1994). Refinement of the crystal structure of cronstedtite-3*T*. *Clays and Clay Minerals, 42*, 544–551.

Song, Y., Jiang, G., Chen, Y., Zhao, P., & Tian, Y. (2017). Effects of chloride ions on corrosion of ductile iron and carbon steel in soil and environments. *Scientific Reports, 7*, 6865.

Steadman, R., & Nuttall, P. M. (1964). Further polymorphism in cronstedtite. *Acta Crystallographica, 17*, 404–406.

Tomeoka, K., & Buseck, P. R. (1985). Indicators of aqueous alteration in CM carbonaceous chondrites: Microtextures of a layered mineral containing Fe, S, O and Ni. *Geochimica et Cosmochimica Acta, 49*, 2149–2163.

Tosca, N. J., Guggenheim, S., & Pufahl, P. K. (2016). An authigenic origin for Precambrian greenalite: implications for iron formation and the chemistry of ancient seawater. *GSA Bulletin, 128*, 511–530.

Van Lier, J. A., De Bruyn, P. L., & Overbeek, J. T. G. (1960). The solubility of quartz. *The Journal of Physical Chemistry, 64*, 1675–1682.

Wahle, M. W., Bujnowski, T. J., Guggenheim, S., & Kogure, T. (2010). Guidottiite, the Mn-analogue of cronstedtite: a new serpentine-group mineral from South Africa. *Clays and Clay Minerals, 58*, 364–376.

Wilson, J., Cressey, G., Cressey, B., Cuadros, J., Ragnarsdottir, K. V., Savage, D., & Shibata, M. (2006). The effect of iron on montmorillonite stability. (II) Experimental investigation. *Geochimica et Cosmochimica Acta, 70*, 323–336.

Wolery, T.J. & Jove-Colon, C.F. (2004). Qualification of thermodynamic data for geochemical modeling of mineral–water interactions in dilute systems. Rep. ANL-WIS-GS-000003 REV 00, U.S. Dept. of Energy, Washington, DC.

Zega, T. J., & Buseck, P. R. (2003). Fine-grained-rim mineralogy of the Cold Bokkeveld CM chondrite. *Geochimica et Cosmochimica Acta, 67*, 1711–1721.

Zolensky, M.E. (1984). Hydrothermal alteration of CM carbonaceous chondrites; implications of the identification of tochilinite as one type of meteoritic PCP. In: *47th Annual Meeting of the Meteoritical Society*, p. 19.

Zolensky, M. & Keller, L.P. (1999). Clay Minerals. In Primitive Meteorites and Interplanetary Dust I. In *Program and Abstracts for Clay Minerals Society 28th Annual Meeting*, p. 184.

Zolensky M. & McSween H.Y. (1988). Aqueous alteration. Pp. 114–143 in: *Meteorites and the Early Solar System* (J.F. Kerridge and M.S. Matthews, editors). University of Arizona Press.

Zolotov, M. Y. (2014). Formation of brucite and cronstedtite bearing mineral assemblages on Ceres. *Icarus, 228*, 13–26.

(*Received 17 January 2020; revised 15 May 2020; AE: F. Javier Huertas***)**